Faculty of Physics and Astronomy

University of Heidelberg

Diploma thesis

in Physics

submitted by

Timo Bastian Ottenstein

born in Eberbach

2006

A New Objective for High Resolution Imaging of Bose-Einstein Condensates

This diploma thesis has been carried out by
Timo Bastian Ottenstein at the
Kirchhoff Institute of Physics
under the supervision of
Prof. Dr. M. K. Oberthaler

Ein neues Objektiv zur hochauflösenden Abbildung von Bose-Einstein Kondensaten

Im Rahmen dieser Arbeit wurde ein neues Abbildungssystem zur Messung der atomaren Dichteverteilung in Bose-Einstein Kondensaten aufgebaut und charakterisiert. Die erreichte optische Auflösung von 1.1 μm nach dem Rayleigh Kriterium bietet nun die Möglichkeit Effekte auf der Skala der sogenannten 'healing Länge' zu untersuchen. Diese 'healing Länge' ist eine Konsequenz der Wechselwirkung zwischen den Einzelatomen und gibt die charakteristische Größenordnung an, auf der sich Variationen in der Dichteverteilung innerhalb des Kondensats vollziehen. Ein bekannter Effekt auf dieser Skala sind dunkle Solitonen, welchen nichtdispersive Strukturen im Kondensat entsprechen. Im zweiten Teil dieser Arbeit wird ein Experiment zur Erzeugung dunkler Solitonen mit Hilfe eines Bose-Einstein Kondensats in einem Doppelmuldenpotential vorgestellt und erste Ergebnisse analysiert.

A New Objective for High Resolution Imaging of Bose-Einstein Condensates

In the framework of this thesis a new imaging system for the measurement of the atomic density distribution in Bose-Einstein condensates has been built and characterized. The achieved optical resolution of 1.1 μm according to the Rayleigh criterion makes it now possible to observe structures on the scale of the so-called 'healing length'. This 'healing length' is a consequence of the interaction between the atoms and gives the typical order of magnitude on which density variations in the condensate occur. A known effect on this scale are dark solitons, being non-dispersive structures in the condensate. In the second part of this thesis an experiment for the generation of dark solitons with the help of a Bose-Einstein Condensate in a double-well potential is presented and first results are discussed.

Contents

Fundamental Constants

Quantity	Symbol	Value	Unit
Speed of light	c	$2.99792458 \cdot 10^{8}$	m s^{-1}
Boltzmann Constant	k_B	$1.3806503(24) \cdot 10^{-23}$	J K^{-1}
Planck Constant	h	$6.62606876(52) \cdot 10^{-34}$	J s
	$h/2\pi$	$1.054571596(82) \cdot 10^{-34}$	J s
	k_B/h	20.836644(36)	Hz nK^{-1}
Specific Data on Rubidium-87			
Mass	m	$1.4445 \cdot 10^{-25}$	kg
s-Wave Scattering Length	a	5.32	nm
Saturation Intensity	I_{sat}	1.58	mW cm^{-2}
D2-Line Width	Γ	$2\pi \times 6.065$	MHz

1 Introduction

Our view of the world is predominantly established by those parts of the world which are directly accessible with our senses. All the more, what is often popularly called the 'microcosmos', bears many surprises for us. The most counterintuitive phenomena arise from quantum mechanics, describing the physical laws on length scales of atoms or elementary particles. The idea of a deterministic theory has to be given up, substituted by the introduction of probability amplitudes. This leads to new effects as e.g. the wave-like character and thus interference of particles, which was first demonstrated by Davisson and Germer in 1927 [1], by investigating the diffraction of electrons at a nickel crystal. This behaviour of seemingly massive particles can be explained by ascribing a wavelength to them that depends on their momentum. Such a concept was already developed by Louis DeBroglie in 1924 [2]. Another effect not known in the macroscopic world is the tunnelling of particles through classically forbidden regions. The detection of tunneling occurs in most cases indirectly, e.g. in Josephson junctions [3, 4] known from solid state physics. These junctions consist of two superconductors separated by a thin insulating barrier. Tunneling of Cooper pairs through this barrier is revealed by a current flowing although no voltage is applied to the junction, as long as electrons are delivered by an external current source. So the question arises if systems can be found in which quantum mechanical effects can be observed directly. This question can be affirmed. Bose-Einstein Condensates (BEC) turned out to be perfect model systems for the observation of quantum mechanical effects on a macroscopic length scale. Macroscopic means here on the micrometer range, but this is accessible with the help of a microscope.

The phenomenon of Bose-Einstein Condensation was theoretically predicted for massive particles by Albert Einstein [5] in 1924 who was inspired by the work of Satyendra Nath Bose [6] on photons one year before. Following their considerations a large number of bosons (particles with integer spin) can occupy the same quantum state, so that the hole atomic ensemble can be described by one single macroscopic wavefunction. The prototype of a Bose-Einstein Condensate is superfluid ^{4}He or ^{3}He. In the case of ^{3}He pairs of fermions form the condensate, similar to the situation in superconductors where the condensing bosons are pairs of electrons. Due to the strong interaction between the particles, even at $T = 0$ the condensate fraction in He liquids is only about 10% or even less. This lead to the search for systems in which interaction is weaker and thus the condensate fraction bigger. Dilute gases turned out to be well suited candidates, although the cooling of such samples is techniquelly a big challenge and new methods of cooling atoms e.g. laser cooling had to be developed until the first Bose-Einstein Condensate in dilute gases could be accomplished by Wiemann, Cornell, Hulet and

Ketterle in 1995 [7, 8, 9].
The interference of matterwaves can be impressively demonstrated with BECs. This was for the first time done by Andrews et al. in 1997 [10]. They created two BECs in a double well potential, after switching off all confining potentials the wave packets expanded, overlapped and formed clear interference fringes with high visibility, demonstrating the wave-like behaviour of massive particles. In the presence of a tunneling coupling between the two condensates these interference patterns, or more accurate their shot to shot fluctuations, can even be utilized for thermometry of ultra low temperatures [11, 12, 13] and a measurement of the heat capacity of a degenerate bose gas. Also the tunnelling of particles was demonstrated in a double well potential [14]. An initial imbalance in the population of the two wells leads to an oscillatory tunnelling dynamics of particles from one well to the other. In this experiment it was for the first time possible to look directly at tunnelling processes with a microscope.
These are only examples of the rich variety of effects that can be studied using Bose-Einstein Condensates. In all cases the acquired information is deduced from pictures of the atom distribution. Consequently, the imaging system is one of the decisive parts of a BEC experiment. In order to get the maximum amount of information from an image, the resolution should be as high as possible. Ideally, it is on the order of the so-called *healing length* which is a result of the interatomic interaction and gives the typical length scale on which density variations in a BEC occur. This enables the direct observation of e.g. vortices or dark solitons [15]. The development of an imaging system fulfilling these requirements is the main subject of the thesis at hand. Suggestions for an objective lens with high numerical aperture are also given in [16, 17], but our design achieves an even higher value.

Generation of Dark Solitons Fans

In standard textbooks on statistical mechanics [18] Bose-Einstein Condensation is always discussed in the framework of ideal gases, i.e. without interaction between single particles. But interaction gives rise to new phenomena, among them solitons. The character of solitary waves is that they maintain their shape under temporal evolution. One can distinguish two different types of solitons. Bright solitons corresponding to a non-dispersive matterwave packet, where dispersion is compensated for by attractive interaction between the particles and dark solitons which are a reduction of the density with respect to its bulk value. This structure is stable due to a balance of the interaction trying to decrease the minimum in density and a phase gradient trying to enhance it. Dark solitons have already been generated with a phase imprinting method [19, 20, 21]. The last chapter of this thesis also deals with the generation of dark solitons. In this work the solitons are created by interference of two matterwave packets in an optical dipole trap [22]. The resultant interference minima are formed into dark solitons due to interaction. The presented experimental results are of preliminary character. This measurement should be repeated when the new imaging system is installed. The higher resolution will make quantitative measurements possible.

Contents of this Thesis

This thesis is divided into three main parts. In chapter two I give an introduction into the theory of imaging. In most imaging system lenses play a major role. Hence, the first two subsections focus on basic properties of lenses, especially their influence on an incident wavefront and their ability to form fourier transforms of an object placed in the focal plane. These considerations will enable us to understand how an image is formed by a lens. We will see, that the image of a given object can be calculated by a convolution with the so called *Point Spread Function* (PSF) which is the response of the imaging system on a single point (δ-excitation) in the object plane. For a circular pupil of the system this PSF is given by an Airy Function determining the resolution and is therefore crucial for the imaging quality. Another way to evaluate the quality of imaging systems is their ability to transfer spatial frequencies. Although such an analysis has not been performed during this thesis, some theory of frequency response is discussed as it gives a deep insight into the theory of imaging. It follows a description of the five most important lens errors. Some of them are also demonstrated with our new objective. To finish this chapter an overview over techniques of imaging a Bose-Einstein Condensate is given.
Chapter three is devoted to the new objective built during this thesis. After a short motivation, why an extension of the current setup is necessary, I will present the lens data and describe the mount accommodating them. In order to specify the quality of the new imaging setup various test measurements including the CCD camera have been performed, whose results establish the main part of this chapter. To conclude this part a plan how to install the objective in the experimental setup is presented.
The fourth chapter deals with the generation of dark soliton fans in Bose-Einstein Condensates. After an introduction into the basic theory of dark solitons the results of a preliminary measurement are given. The Appendix contains technical drawings for all components the objective consists of.

2 Theory of Imaging

The most important components of common imaging systems are, of course, lenses. Before we devote ourselves to the new imaging setup developed during this thesis, some lens theory and the theory of image formation are discussed. We will see that there is an easy mathematical connection between object and image in form of a convolution of the object with a function called Point Spread Function (PSF), whose form is crucial for the quality of the imaging. Differences between coherent and incoherent illumination of the sample will be discussed, as well as the influence of lens aberrations. Finally, an overview over techniques for imaging a Bose-Einstein Condensate (BEC) will be given.

2.1 Phase Transforming Properties of Lenses and Paraxial Approximation

As well known, lenses are made of an optically dense material with usually spherical surfaces. The effect of a lens on an incident light ray depends on the refractive index and on the shape of the lens' surfaces. There are several types of lenses, only a small selection is shown in Figure 2.1.

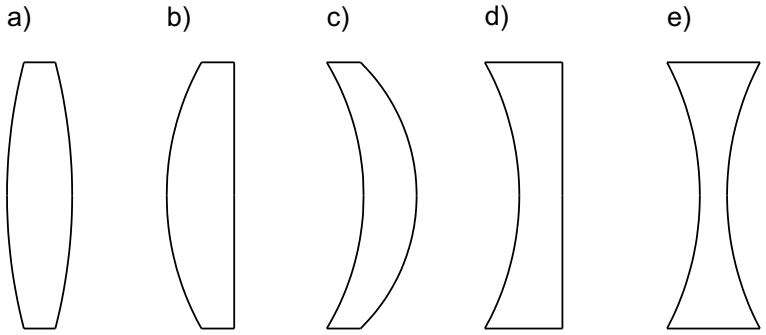

Figure 2.1: A small selection of lens types: a) bi-convex b) plano-convex c) positive meniscus d) plano-concave e) bi-concave

In principle, a lens imprints a position dependent phase delay on the incident light. The phase delay is given by:

$$\Phi(x,y) = kn\Delta(x,y) + k\left(\Delta_0 - \Delta(x,y)\right) \tag{2.1}$$

Δ_0 is the maximum thickness of the lens; $\Delta(x, y)$ describes the thickness of the lens in a plane perpendicular to the optical axis; n is the refractive index of the lens material

For a bi-convex lens as shown in Figure 2.1, with radii R1 (left side) and R2 (right side), the thickness function can easily be calculated as:

$$\Delta(x,y) = \Delta_0 - R_1\left(1 - \sqrt{1 - \frac{x^2+y^2}{R_1^2}}\right) + R_2\left(1 - \sqrt{1 - \frac{x^2+y^2}{R_2^2}}\right) \tag{2.2}$$

where R_1 is taken positive and R_2 negative due to the usual sign convention that surfaces which are curved to the left side have a positive radius and surfaces curved to the right side have a negative radius. The light ray is always assumed to travel from left to right.

In many situations it is possible to simplify expression (2.2) significantly. This approximation is valid when considering only parts of the wavefront that are close to the optical axis. Then the square root can be expanded in a Taylor series up to second order:

$$\sqrt{1 - \frac{x^2+y^2}{R_{1/2}^2}} \approx 1 - \frac{x^2+y^2}{2R_{1/2}^2} \tag{2.3}$$

This expansion is called paraxial approximation. Substituting (2.3) into the thickness function (2.2) yields:

$$\Delta(x,y) = \Delta_0 - \frac{x^2+y^2}{2}\left(\frac{1}{R_1} - \frac{1}{R_2}\right) \tag{2.4}$$

Together with (2.1) the influence of the lens on the incident wavefront can mathematically be expressed as a multiplicative phase. Let $U_0(x, y)$ be the (complex) amplitude of the incident wave, then the field right after the lens $U'(x, y)$ is given by:

$$U'(x,y) = P(x,y)\exp\left(ikn\Delta_0\right)\exp\left(-ik\frac{x^2+y^2}{2f}\right)U_0(x,y) \tag{2.5}$$

where the refractive index and the radii of the lens surfaces have been absorbed in the focal length f which is defined as $1/f := (n-1)\left(\frac{1}{R_1} - \frac{1}{R_2}\right)$. $P(x, y)$ is called pupil function and describes the finite aperture of the lens.

$$P(x,y) = \begin{cases} 1 & \text{, within the aperture} \\ 0 & \text{, outside of the aperture} \end{cases} \tag{2.6}$$

The physical meaning of (2.5) is most obvious in the case of a plane wave with an unitary amplitude so that $U_0(x, y) = 1 \,\forall\, x, y$. For $f > 0$ this corresponds to a parabolic approximation to a spherical converging wave, while for $f < 0$ the wave is diverging. These results may give rise to the assumption that a lens with perfect spherical surfaces

generates a perfect spherical wavefront which converges in one single point. On the one hand, the consideration rely on the applicability of the paraxial approximation which is only possible in a region near the optical axis, on the other hand a focus consisting of one single point is physically not possible as the intensity would be infinity in the focus. The finite aperture of the lens rather limits the spot size in the focus due to diffraction effects. The resulting pattern is described by an Airy function as we will see later. In practice, lenses are often aspherically corrected in order to produce a wavefront resembling a sphere as good as possible, or many spherical lenses are used to compensate the aberrations of one lens with the aberrations of the other ones.

2.2 A Lens as a Fourier Transformer

In this part it will be shown that a convex lens acts as an exact Fourier transformer for an object which is placed in its focal plane. First the more general case that the object is placed at a distance d in front of the lens and can be described by the (complex) field amplitude $U_0(x_0, y_0)$ is considered. In the following the Fresnel diffraction formula will be used, which describes the free propagation of a field amplitude $U_0(x, y)$ over a distance z. The resulting field is then given by

$$U'(x', y') = \frac{\exp(ikz)}{i\lambda z} \int dx\, dy\, U_0(x, y) \exp\left(i\frac{k}{2z} \left[(x' - x)^2 + (y' - y)^2 \right] \right) \tag{2.7}$$

A derivation of this formula can be found in [23] or [24]. One can interpret this expression as a convolution of the incident wavefront with an exponential function. According to the convolution theorem [25] a convolution in real space corresponds to a multiplication in Fourier space[1]. For this reason it is useful to write down the Fourier transform of the exponential function in (2.7). This yields the following transfer function

$$H(f_x, f_y) = \exp(ikz) \exp\left[-i\pi\lambda z (f_x^2 + f_y^2) \right] \tag{2.8}$$

with $f_x = \frac{x'}{\lambda f}$ and $f_y = \frac{y'}{\lambda f}$. The special choice of the spatial frequency will be clear later. This transfer function connects the Fourier transform of the incident field $F(f_x, f_y)$ with the Fourier transform of the propagated field via

$$F'(f_x, f_y) = H(f_x, f_y) \times F(f_x, f_y). \tag{2.9}$$

We are interested in the resulting field amplitude in the back focal plane of the lens. Assuming that the field $U_l'(x, y)$ right after the lens is known, the field distribution $U_f(x_f, y_f)$ in the focal plane is given by applying (2.7)

[1] $\int_{-\infty}^{\infty} d\tau f(t)g(t - \tau) = \mathcal{F}^{-1}\left(\mathcal{F}(f) \cdot \mathcal{F}(g)\right)$

$$
\begin{aligned}
U_f(x_f, y_f) =& \frac{1}{i\lambda f} \exp\left[i \frac{k}{2f} (x_f^2 + y_f^2) \right] \\
& \int dx\, dy\, U_l'(x, y) \exp\left[i \frac{k}{2f} (x^2 + y^2) \right] \exp\left[-i \frac{2\pi}{\lambda f} (x x_f + y y_) \right].
\end{aligned}
\tag{2.10}
$$

The constant phase factor $\exp(ikf)$ was dropped. Using equation (2.5) one can rewrite (2.10)

$$
U_f(x_f, y_f) = \frac{1}{i\lambda f} \exp\left[i \frac{k}{2f} (x_f^2 + y_f^2) \right] \underbrace{\int dx\, dy\, U_l(x, y) \exp\left[-i \frac{2\pi}{\lambda f} (x x_f + y y_f) \right]}_{F_l(f_x, f_y)} \tag{2.11}
$$

where I have neglected the phase factor $\exp(ikn\Delta_0)$ and the finite aperture size of the lens. This is satisfied if the diameter of the lens is much bigger than the spatial extend of the imaged object. The integral expression is simply the Fourier transformation of the field amplitude in the front plane of the lens, which suggests the application of the transfer function given in (2.8) yielding after some algebra our final result

$$
U_f(x_f, y_f) = \frac{1}{i\lambda f} \exp\left[-\frac{k}{2f} \left(1 - \frac{d}{f} (x_f^2 + y_f^2) \right) \right] F_0\left(\frac{x_f}{\lambda f}, \frac{y_f}{\lambda f} \right) \tag{2.12}
$$

or in detail

$$
\begin{aligned}
U_f(x_f, y_f) =& \frac{1}{i\lambda f} \exp\left[i \frac{k}{2f} \left(1 - \frac{d}{f} \right) (x_f^2 + y_f^2) \right] \\
& \int dx\, dy\, U_0(x_0, y_0) \exp\left[-i \frac{2\pi}{\lambda f} (x_0 x_f + y_0 y_f) \right]
\end{aligned}
\tag{2.13}
$$

For $d = f$ the prefixed phase factor vanishes and the resulting field amplitude equals the exact Fourier transformation of the imaged object. In this derivation the finite aperture of the lens was neglected. In real situations the aperture stop leads to the so called vignetting effect, as for one point in the back focal plane not the whole object contributes but only that part which corresponds to the region from which light is collected by the lens.

2.3 The Point Spread Function

A very important feature of lenses is their ability to form images i.e. if an object is located in a plane in front of a lens an intensity distribution resembling the object is reproduced in a plane different to the object plane (see Figure 2.2). With the considerations done in the two previous chapters we are now in the position to get a deeper insight in the process of image formation. For simplicity I will first assume an aberration-free thin lens and monochromatic coherent illumination leading to a linear relation between image and object. So the interesting question is, what the image of a point-like object looks like. The superposition principle allows then to calculate the image of arbitrary shapes by evaluation of the integral

$$U_1(x_1, y_1) = \int dx_0\, dy_0\, h(x_1, y_1; x_0, y_0) U(x_0, y_0). \tag{2.14}$$

$h(x_1, y_1; x_0, y_0)$ is the so called point spread function (PSF) whose calculation is straight forward. Let us imagine a point source located at $\mathbf{r_0}$ which is emitting a spherical wave.

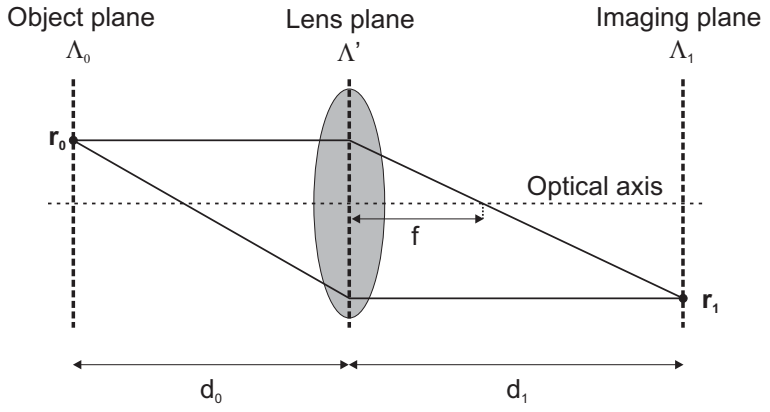

Figure 2.2: Planes and notation for image formation

The normalised field at the point $\mathbf{r}'$ in the lens plane is then given by[2]:

$$U(\mathbf{r}', \mathbf{r_0}) = \frac{\exp\left(ik|\mathbf{r}' - \mathbf{r_0}|\right)}{i\lambda|\mathbf{r}' - \mathbf{r_0}|}. \tag{2.15}$$

Applying the paraxial approximation and using full coordinate notation this expression reads ($z_0 := 0$)

$$U(x', y'; x_0, y_0) = \frac{1}{i\lambda d_0} \exp\left[\frac{ik}{d_0}\left(d_0^2 + \frac{(x' - x_0)^2}{2} + \frac{(y' - y_0)^2}{2}\right)\right]. \tag{2.16}$$

[2]The factor $1/i\lambda$ is introduced to be consistent with the Fresnel diffraction formula. In a detailed derivation it emerges because of the introduction of imaginary secondary sources. For further reading refer to [23].

As described in section 2.1 the lens imprints a parabolic phase (2.5) and the propagation to the distance d_1 after the lens is done by using the Fresnel formula (2.7). This leads to the lengthy result:

$$\begin{aligned} U(x_1, y_1; x_0, y_0) =& \frac{1}{\lambda^2 d_0 d_1} \underbrace{\exp\left[i\frac{k}{2d_1}(x_1^2 + y_1^2)\right]}_{(1)} \underbrace{\exp\left[i\frac{k}{2d_0}(x_0^2 + y_0^2)\right]}_{(2)} \\ & \int dx'\, dy'\, P(x', y') \underbrace{\exp\left[i\frac{k}{2}\left(\frac{1}{d_0} + \frac{1}{d_1} - \frac{1}{f}\right)(x'^2 + y'^2)\right]}_{(3)} \\ & \exp\left\{-ik\left[\left(\frac{x_0}{d_0} + \frac{x_1}{d_1}\right)x' + \left(\frac{y_0}{d_0} + \frac{y_1}{d_1}\right)y'\right]\right\} =: h(x_1, y_1; x_0, y_0). \end{aligned} \tag{2.17}$$

Most disturbing in (2.17) are the quadratic phase factors (1)-(3) as indicated in equation (2.17). Fortunately, they can be eliminated by the following reasons:

(1) This is a pure phase factor in the imaging plane, independent on the coordinates of the object. Since most detectors are only sensitive on intensity this factor can be dropped immediately.

(2) To neglect this factor a more detailed argumentation is necessary, because it is dependent on coordinates in the object plane which are integration variables in (2.14). In the case of a good imaging system, only a small region in the object plane contributes to the image at the point (x_1, y_1). Then one can approximate:

$$\exp\left[i\frac{k}{2d_0}(x_0^2 + y_0^2)\right] \approx \exp\left[i\frac{k}{2d_0}\frac{x_1^2 + y_1^2}{M^2}\right] \tag{2.18}$$

where M is the magnification. Now this factor can be neglected for the same reasons as above.

(3) From geometric optics the lens law

$$\frac{1}{f} = \frac{1}{d_0} + \frac{1}{d_1} \tag{2.19}$$

is known. It connects the focal length of the lens with the distances from object (d_0) and imaging plane (d_1). So this phase factor is equal to one and can also be omitted.

By defining the magnification of the imaging system as $M = -\frac{d_1}{d_0}$ (the minus sign represents the inverting property of the imaging), and $(\tilde{x}/\tilde{y})_0 = M(x/y)_0$, one can write the PSF as:

$$\begin{aligned} h(x_1, y_1; \tilde{x_0}, \tilde{y_0}) &= \frac{1}{\lambda^2 d_0 d_1} \int dx'\, dy'\, P(x', y') \exp\left\{-i\frac{k}{d_1}\left[(\tilde{x_0} - x_1)x' + (\tilde{y_0} - y_1)y'\right]\right\} \\ &= h(\tilde{x_0} - x_1, \tilde{y_0} - y_1) \end{aligned} \tag{2.20}$$

I apply a second coordinate transformation, now concerning the coordinates in the lens plane

$$u = \frac{x'}{d_1\lambda} \quad \text{and} \quad v = \frac{y'}{d_1\lambda} \tag{2.21}$$

which results in

$$h(\tilde{x_0} - x_1, \tilde{y_0} - y_1) = M \int du\, dv\, P(\lambda d_1 u, \lambda d_1 v) \exp\left\{-i2\pi\left[u(\tilde{x_0} - x_1) + v(\tilde{y_0} - y_1)\right]\right\}. \tag{2.22}$$

We see that the PSF is shift invariant depending only on the difference of $(\tilde{x}, \tilde{y})_0 - (x, y)_1$, which makes the relation between object and image mathematically interpretable as a convolution.

So the integral (2.14) can be written as

$$U_1(x_1, y_1) = \frac{1}{M^2} \int d\tilde{x_0}\, d\tilde{y_0}\, h(\tilde{x_0} - x_1, \tilde{y_0} - y_1) U_0\left(\frac{\tilde{x_0}}{M}, \frac{\tilde{y_0}}{M}\right) \tag{2.23}$$

From this expression it is clear that the image is smoothed out with the point spread function. The broader the PSF the more details are lost in the image. For a good imaging system the PSF should resemble a delta function as good as possible.

The point spread function (2.22) is physically interpretable as the Fraunhofer diffraction of a circular aperture of the size of the lens. For an evaluation of this integral see e.g. [23]. The result is the so called Airy function, which is radially symmetric and given by

$$h(r) \propto \frac{2J_1(kaMr/d_1)}{kaMr/d_1} \tag{2.24}$$

where a is the radius of the lens and J_1 is the Bessel function of first kind.

The absolute square of (2.24) is the intensity distribution a point-like object produces in the imaging plane (scaled in units of the object plane).

$$I(r) \propto \left| \frac{2J_1(kaMr/d_1)}{kaMr/d_1} \right|^2 \tag{2.25}$$

An example is plotted in Figure 2.3 a).

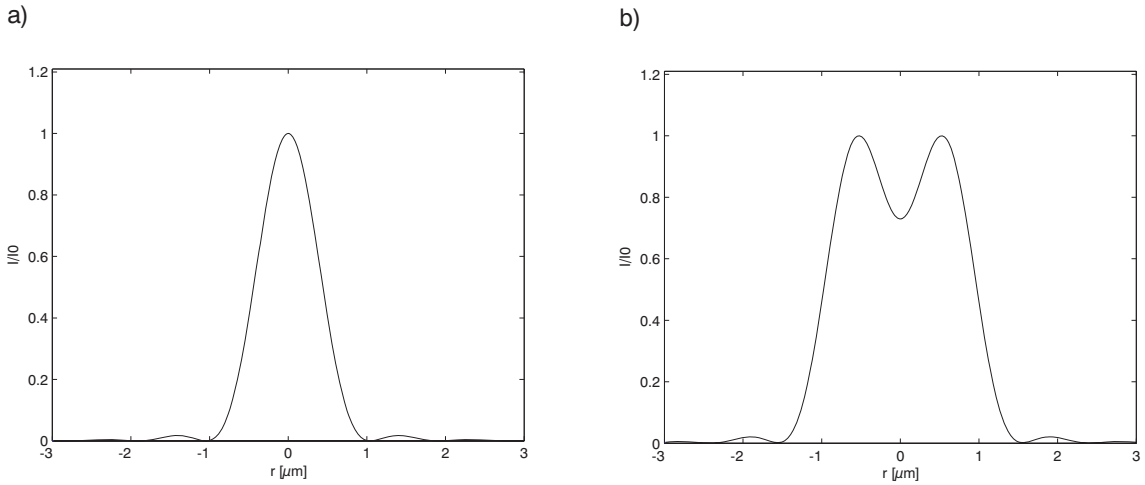

Figure 2.3: a) Example of a normalized PSF for $\lambda = 780$ nm,$a = 1$ cm and a working distance of $d_0 = 2.2$ cm. The resolution is approximately 1.1 μm b) Incoherent image of two points separated by the Rayleigh distance (For this example the parameters of the new imaging setup have been used)

This function determines the resolution of the imaging system. Commonly resolution is defined as the minimum distance which two points may have, so that they are still separated in the image. According to the *Rayleigh criterion* this minimum distance is the distance between the central maximum and the first minimum of (2.25). The first minimum of the Airy function is located at 1.22π. This leads to the following equation for the resolution

$$\frac{ka|M|\Delta r_{Rayleigh}}{d_1} = 1.22\pi \Rightarrow \Delta r_{Rayleigh} = \frac{0.61\lambda d_0}{a}. \tag{2.26}$$

Figure 2.3 b) shows the incoherent image (differences between coherent and incoherent illumination will be discussed later) of two point objects separated by the Rayleigh distance. The plot shows a clear minimum in the middle. Consequently, the Rayleigh criterion is a pessimistic estimation of the resolution, since even for smaller distances the two points will be observed separately. At a certain distance this minimum will vanish and only a single intensity peak is visible. This distance corresponds to the resolution according to the *Sparrow criterion*. In this case the resolution is given by

$$\Delta r_{Sparrow} = \frac{0.47\lambda d_0}{a} \tag{2.27}$$

and amounts about 75% of the value according to the Rayleigh criterion.

These considerations did not take into account any lens aberrations and describes only the behaviour of so-called *diffraction-limited* systems. The influence of aberrations will be discussed later in this chapter, see section 2.5.

2.4 Frequency Response of an Imaging System

The quality of an imaging system cannot only be evaluated by analysing the image of very small objects. Another standard technique is to investigate how spatial frequencies are transferred by the system. Although such an analysis has not been performed during this thesis, it is worthwhile having a look on the theory of frequency response.

2.4.1 Coherent Illumination

As shown in the previous section the image forming process can mathematically be described by the convolution

$$U_1(x_1, y_1) = \int d\tilde{x_0}\, d\tilde{y_0}\, \tilde{h}(\tilde{x_0} - x_1, \tilde{y_0} - y_1) U_g(\tilde{x_0}, \tilde{y_0}) \tag{2.28}$$

with the abbreviations

$$\tilde{h} = \frac{h}{M} \quad \text{and} \quad U_g(\tilde{x_0}, \tilde{y_0}) = \frac{1}{M} U_0\left(\frac{\tilde{x_0}}{M}, \frac{\tilde{x_0}}{M}\right). \tag{2.29}$$

In section 2.2 it has already been made use of the convolution theorem which is also applicable here. The frequency spectra of the object and the image are given by the Fourier transform of U_1 and U_g

$$\begin{aligned} F_g(f_x, f_y) &= \int d\tilde{x_0}\, d\tilde{y_0}\, U_g(\tilde{x_0}, \tilde{y_0}) \exp\left[-i2\pi(f_x\tilde{x_0} + f_y\tilde{y_0})\right] \\ F_1(f_x, f_y) &= \int dx_1\, dy_1\, U_1(x_1, y_1) \exp\left[-i2\pi(f_x x_1 + f_y y_1)\right] \end{aligned} \tag{2.30}$$

The Fourier transform of the PSF is called *Coherent Transfer Function* (CTF).

$$H(f_x, f_y) = \int dx_1\, dy_1\, \tilde{h}(x_1, y_1) \exp\left[-i2\pi(f_x x_1 + f_y y_1)\right] \tag{2.31}$$

The convolution theorem tells us how these Fourier transforms are connected

$$F_1(f_x, f_y) = H(f_x, f_y) \times F_g(f_x, f_y) \tag{2.32}$$

According to (2.22) the PSF is itself the Fourier tranform of the pupil function of the imaging system. The CTF can consequently be written as

$$H(f_x, f_y) = \mathcal{F}\left(\mathcal{F}\left(P(\lambda M d_0 \tilde{x}, \lambda M d_0 \tilde{y})\right)\right) = P(-\lambda d_1 f_x, -\lambda d_1 f_y) \tag{2.33}$$

This expression gives a deep insight into the frequency response of a diffraction limited imaging system. The pupil function was defined as 1 inside the aperture of the imaging lens and zero outside. Thus this function has the same value at each point inside the aperture and drops suddenly to zero at the margin of the lens. These properties are directly transferred to the CTF. For a circular aperture all spatial frequencies which are smaller than the cut-off frequency will be transferred without any perturbation while frequencies bigger than the cut-off frequency cannot pass the imaging system.

For a lens aperture with radius a the cutoff frequency is given by the equation

$$\lambda d_1 f_{\text{cutoff}} = a \quad \Rightarrow \quad f_{\text{cutoff}} = \frac{a}{\lambda M d_0} \tag{2.34}$$

for our example in Figure 2.3 and an elevenfold magnification the cutoff frequency is

$$f_{\text{cutoff}} = \frac{1\text{cm}}{780\text{nm} \times 11 \times 2.2\text{cm}} \approx 52 \frac{\text{cycles}}{\text{mm in the imaging plane}} \tag{2.35}$$

2.4.2 Incoherent Illumination

In the last subsection our considerations were focused on a coherent illumination of the object. We saw that the mathematical description is linear in the (complex) field amplitude, in the incoherent case this description is linear in intensity. The intensity in the imaging plane is therefore given by

$$I_1(x_1, y_1) = \int d\tilde{x_0}\, d\tilde{y_0} \left|\tilde{h}(\tilde{x_0} - x_1, \tilde{y_0} - y_1)\right|^2 I_g(\tilde{x_0}, \tilde{y_0}). \tag{2.36}$$

Following the same steps as in the previous subsection, one can write this expression again as a multiplication in Fourier space (in the incoherent case calligraphic letters will be used for the Fourier transforms)

$$\mathcal{G}_1(f_x, f_y) = \mathcal{H}(f_x, f_y) \times \mathcal{G}_g(f_x, f_y). \tag{2.37}$$

The only difference to the already discussed case is that now the normalized frequency spectra are used

$$\mathcal{H}(f_x, f_y) = \frac{\int dx\, dy \left|\tilde{h}(x, y)\right|^2 \exp\left[-i2\pi(f_x x + f_y y)\right]}{\int dx\, dy \left|\tilde{h}(x, y)\right|^2} \tag{2.38}$$

The normalization by the zero frequency component is done for a physical reason. The information contained in an image is to a large extent dependent on the ratio of the Fourier coefficients of higher frequencies to the zero frequency background, which is also interpretable as the contrast with which a certain frequency is transferred by the imaging system. The function $\mathcal{H}(f_x, f_y)$ is called *Optical Transfer Function* (OTF) and is in general complex valued. Its absolute value $|\mathcal{H}|$ is known under the name of *Modulation Transfer Function* (MTF) and its phase part is called *Phase Transfer Function* (PTF).

There are some general properties of the OTF which should be mentioned here [23]:

1. $\mathcal{H}(0,0) = 1$
2. $\mathcal{H}(-f_x, -f_y) = \mathcal{H}^*(f_x, f_y)$
3. $|\mathcal{H}(f_x, f_y)| \leq |\mathcal{H}(0,0)|$

Since both the CTF and the OTF can be calculated from the PSF $\tilde{h}$ it is not astonishing that there is a relation between them:

$$\mathcal{H}(f_x, f_y) = \frac{\int d\xi\, d\eta\, H\left(\xi + \frac{f_x}{2}, \eta + \frac{f_y}{2}\right) H^*\left(\xi - \frac{f_x}{2}, \eta - \frac{f_y}{2}\right)}{\int d\xi\, d\eta\, |H(\xi, \eta)|^2} \tag{2.39}$$

With (2.39) it is now easy to write down a formula for the OTF of a diffraction limited system. As shown in the previous subsection the CTF is just given by the pupil function of the imaging system (2.33). Thus, it follows

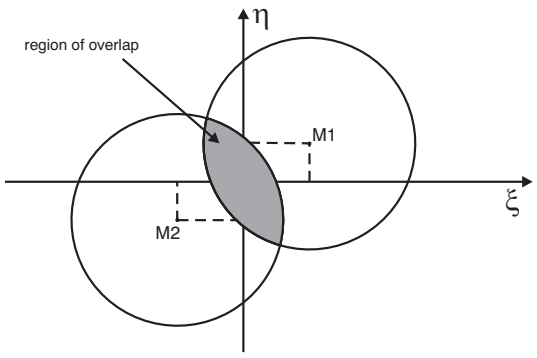

Figure 2.4: Illustration of formula (2.40): The numerator corresponds to the grey shaded overlap area of the two circular pupil functions. From this point of view it is also clear that the OTF of a diffraction limited system with circular aperture is always real an nonnegative. $M1 = \left(\frac{\lambda d_1 f_x}{2}, \frac{\lambda d_1 f_y}{2}\right)$, $M2 = \left(\frac{-\lambda d_1 f_x}{2}, -\frac{\lambda d_1 f_y}{2}\right)$.

$$\mathcal{H}(f_x, f_y) = \frac{\int d\xi\, d\eta\, P\left(\xi - \frac{\lambda d_1 f_x}{2}, \eta - \frac{\lambda d_1 f_y}{2}\right) P\left(\xi + \frac{\lambda d_1 f_x}{2}, \eta + \frac{\lambda d_1 f_y}{2}\right)}{\int d\xi\, d\eta\, P(\xi, \eta)}. \tag{2.40}$$

This formula can be illustrated by geometrical means. The numerator is just the overlap of two pupil functions which are centered at the points $M1 = \left(\frac{\lambda d_1 f_x}{2}, \frac{\lambda d_1 f_y}{2})\right)$ and $M2 = \left(-\frac{\lambda d_1 f_x}{2}, -\frac{\lambda d_1 f_y}{2}\right)$ while the denominator is a normalization by the area of the pupil function. Figure 2.4 depicts the situation for a circular pupil function. Because of symmetry it would be sufficient to set $f_y = 0$, but for clarity the graph shows the general case. Using this geometrical interpretation of (2.40) it is easy to derive an analytical expression for the OTF of a circular pupil, which reads [23]

$$\mathcal{H}(f_x) = \frac{2}{\pi}\left[\arccos\left(\frac{f_x}{f_{ic}}\right) - \frac{f_x}{f_{ic}}\sqrt{1-\left(\frac{f_x}{f_{ic}}\right)^2}\right] \tag{2.41}$$

where $f_{ic} = \frac{2a}{\lambda d_1}$ is the incoherent cutoff frequency. In Figure 2.5 the CTF and the OTF for the parameters of our new objective are shown. Comparison of with (2.34) shows

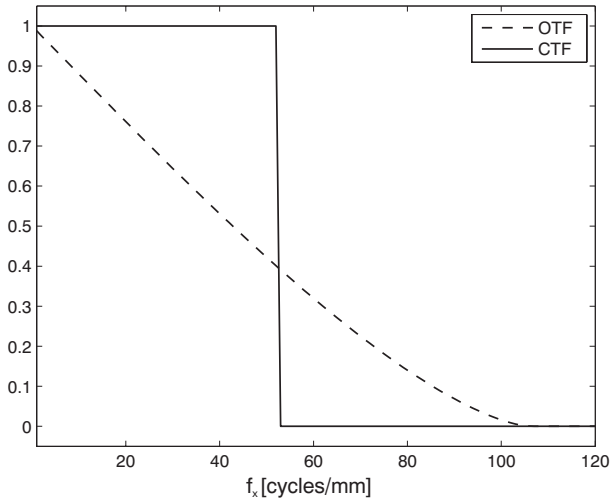

Figure 2.5: *Optical Transfer Function* (dashed line) and *Coherent Transfer Function* (solid line) for $a = 1cm, \lambda = 780nm$, a working distance of $d_0 = 2.2cm$ and an elevenfold magnification. The behaviour is totally different. While the CTF is equal to one up to the coherent cutoff frequency, the OTF decreases continuously. The parameters of our new objective have been used for this diagram. The x-axis refers to cycles/mm in the imaging plane.

that the incoherent cutoff frequency is twice the value of the coherent one. This could suggest that the resolution in the incoherent case is a factor of two better than with coherent illumination, but this is not true in general and depends on the object one wants to image. Let us for example consider the resolution of two points separated by the Rayleigh distance. For incoherent illumination the intensity distribution is shown in Figure 2.3 b). In the coherent case, of course, first the amplitudes have to be added and the absolute square must be taken afterwards. The intensity distribution in the image therefore depends on the relative phase between the two point sources.

$$I(x) = \left| 2\frac{J_1\left(\frac{1.22\pi(x-\Delta r/2)}{\Delta r}\right)}{\left(\frac{1.22\pi(x-\Delta r/2)}{\Delta}\right)} + \exp(i\Phi)\, 2\frac{J_1\left(\frac{1.22\pi(x+\Delta r/2)}{\Delta r}\right)}{\left(\frac{1.22\pi(x+\Delta r/2)}{\Delta}\right)} \right|^2 \tag{2.42}$$

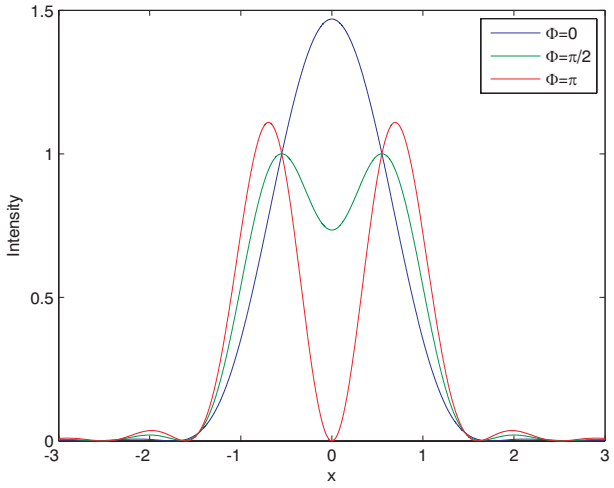

Figure 2.6: Coherent image of two point sources separated by the Rayleigh distance for different phase shifts between them.

Figure 2.6 depicts the image of two point sources which are separated by the Rayleigh distance. We see that the separation depends strongly on the relative phase. For $\Phi = \pi/2$ the result is the same as for illumination with incoherent light, but for phase $\Phi = 0$ one cannot distinguish between the points anymore, while the separation is best for $\Phi = \pi$. This simple example shows that in the case of a coherent light source interferences play a significant role and can decide about the resolving power of the imaging system. Depending on the phase distribution in the object plane they can improve the performance or they can lead to an extensive degradation.

2.5 Lens Aberrations

In the previous sections it was always assumed that the imaging system is diffraction limited and no lens errors are present. In general imperfections of the lens will introduce a disturbance of the wavefront. It was Lord Rayleigh who introduced a criterion for the evaluation of an optical instrument in terms of wavefront distortion. According to him, the image is appreciably blurred when the deviation of the wavefront is more than one fourth of the wavelength for $\lambda = 550$ nm. As lens aberrations are discussed in many textbooks [26, 27] (a more mathematical description can be found in [28]), first a short quantitative discussion of the various types of lens errors is given before considering the influence on the CTF and OTF.

Spherical Aberration

Even if the surfaces of a lens are perfectly spherical not all rays intersect the optical axis at the same point. Rays passing the lens at points on the margin experience a stronger refraction as rays propagating in a region where the paraxial approximation is valid. See Figure 2.7.

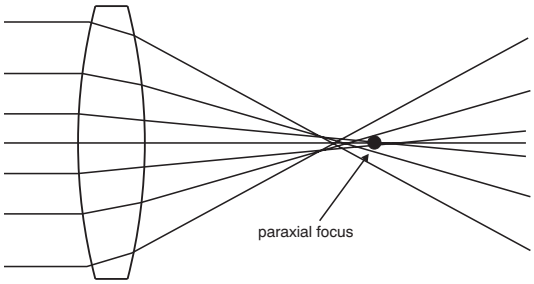

Figure 2.7: Path of rays for a convex lens with spherical surfaces. Rays on the margin of the lens are refracted stronger than rays in the central region where the paraxial approximation is valid, leading to a smearing out of the focus.

As explained in the former sections the intensity distribution in the focus can be described by an Airy pattern. The effect of spherical aberration on this pattern is that light is transferred from the central intensity peak to the outer rings. A deviation of the wavefront of $\lambda/4$ diminishes the intensity in the center about 20%. For some lenses the orientation decides about the amount of spherical aberration. In the case of a plano-convex lens, the plane surface should be oriented to this side where the angle of beamspread is bigger. Hence, for focusing a collimated beam the curved side must face the incoming wave. This can also be seen in the lens configuration of our new objective (Figure 3.1), the third lens is plano-convex and the curved side faces the collimated beam.

Coma

Coma appears in the image of objects which are not centered on the optical axis but laterally shifted. The image of a point-like object exhibits comet tail looking blurrings which increase with the distance from the center. The reasons for this degradation of the imaging quality are similar to the ones of spherical aberration, but now the rays additionally impinge under an angle on the surface of the lens, so that the refraction angle is not symmetric anymore for rays above and below the optical axis. Figure 2.8 shows an image of point-like objects far away from the optical axis. This image was acquired with the test setup (see section 3.4.1) for our new imaging setup built during this thesis.

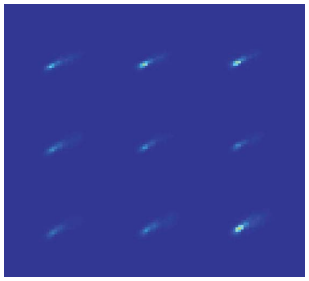

Figure 2.8: Coma aberration for point-like objects approximately 350 μm away from the optical axis. The comet tail form is clearly visible. This image was taken with the test setup for the new objective. These patterns only appear far away from the optical axis, thus this aberration does not diminish the imaging quality in the region of interest. The astigmatism discussed in the following is more critical, see section 3.4.5.

Astigmatism

Another aberration appearing for objects which are not placed on the optical axis is astigmatism. The processes leading to this imaging error are pictured in Figure 2.9.

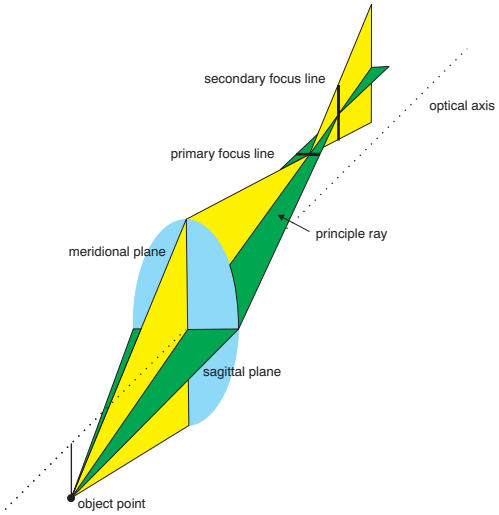

Figure 2.9: Path of rays in case of astigmatism: the formation of the primary and secondary focus lines is clearly visible. The distance between them is called astigmatic difference. Between these two lines the intensity pattern consists of an unsharp circular spot.

One can define two planes being perpendicular to each other. The first one is the meridional plane containing the principle ray and the optical axis, the second one is named sagittal plane and is perpendicular to the meridional plane containing also the principle ray. The principle ray is the ray beginning at the object point and intersecting the lens on the optical axis. Rays lying in the meridional plane are stronger tilted with respect to the lens as rays in the sagittal plane resulting in different focal lengths for these two planes. This leads to a significant deformation of the light cone leaving the lens. Right after the lens it is circular but assumes a more elliptic shape during propagation

whereas the semi-major axis lies in the sagittal plane until the intensity distribution takes the form of a line, the primary focus line. After this point the form changes into an unsharp circular spot, until after some propagation again a line form emerges which is now perpendicular to the first one. This second line is called secondary focus line. The difference between the points where the line forms appear is named astigmatic difference and increases with the distance of the object from the optical axis. In real situations the focus lines are not really lines but complicated diffraction patterns. They resemble a line more and more when the amount of astigmatism increases. Astigmatism also arises when imaging is done through a tilted glass plate, but this error can be corrected with a second glass plate with accurate thickness tilted in the other direction. Since in our setup we also image through a vacuum glass cell the influence of a tilt was also investigated, see section 3.4.7. Figure 2.10 shows once more images of point-like objects, while the imaging was done through a tilted glass plate. This picture was also acquired with the test setup for the new objective.

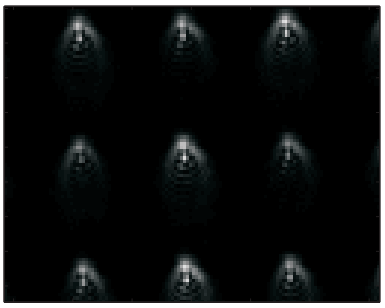

Figure 2.10: Image acquired with the test setup for the new objective, while the glass plate was significantly tilted. The observable structures emerge because of an interplay of coma and strong astigmatism.

Curvature of Field and Distortion

Even when none of the aberrations mentioned above are present, the imaging plane is not really a plane but more a curved manifold. For convex lenses this manifold is curved towards the object plane for regions on the margin of the image. The imaging plane is only flat when the paraxial approximation is valid. This effect is called *Curvature of field* or *Petzval-aberration* and is observable by moving the detector in axial direction. When this aberration plays a role the focus position for objects further away from the optical axis is closer to the lens as for objects in the central part.

The last type of aberration I want to mention here is *distortion*. This effect is reasoned by a variation of the magnification properties of the lens over its surface. This leads to either a pincushion or barrel typed deformation of the image depending on whether the magnification is smaller or bigger on the optical axis in comparison to the outer regions of the lens.

Effects on the Coherent Transfer Function

In section 2.4.1 we saw that the CTF of a diffraction limited imaging system is in principle given by the pupil function. This can be directly transferred to the aberrated case, by introducing a generalized pupil function $\mathcal{P}(x, y)$

$$\mathcal{P}(x, y) = P(x, y) \exp\left[ikW(x, y)\right]. \tag{2.43}$$

where $W(x, y)$ describes an effective path length deviation from the ideal case. The CTF then reads

$$H(f_x, f_y) = P(-\lambda d_1 f_x, -\lambda d_1 f_y) \exp\left[ikW(-\lambda d_1 f_x, -\lambda d_1 f_y)\right] \tag{2.44}$$

The cut-off frequency is obviously not changed by aberrations. The only influence is the introduction of phase distortions within the passband, which can have disastrous effects on the quality of the imaging system.

Effects on the Optical Transfer Function

To find the effects on the OTF one just follows the steps performed in an earlier section by substituting the generalized pupil function (2.43) into (2.40). In order to keep the notation simple I introduce the abbreviations:

$$u_{+/-} = \xi\,(+/-)\,\frac{\lambda d_1 f_x}{2} \quad \text{and} \quad v_{+/-} = \eta\,(+/-)\,\frac{\lambda d_1 f_y}{2} \tag{2.45}$$

Thus the OTF is given by

$$\mathcal{H}(f_x, f_y)_{\text{aberrated}} = \frac{\int d\xi\, d\eta\, P(u_-, v_-) \exp\left[ikW(u_-, v_-)\right]\; P(u_+, v_+) \exp\left[-ikW(u_+, v_+)\right]}{\int d\xi\, d\eta\, P(\xi, \eta)} \tag{2.46}$$

Using this expression as a starting point and applying Schwarz' Inequality [3] it is easy to conclude that

$$\left|\mathcal{H}_{\text{aberrated}}\right|^2 \leq \left|\mathcal{H}_{\text{without aberrations}}\right|^2 \tag{2.47}$$

In other words, lens aberrations always lead to a degradation of the Modulation Transfer Function. The cut-off frequency is not changed, but in general high spatial frequencies suffer from aberrations such that they are extensively suppressed, what leads to the same effects as a decrease of the cut-off frequency. For a diffraction limited system the OTF is always positive. This is not true when aberrations are present. Negative values lead to a contrast reversal, meaning that intensity maxima become minima and vice versa.

[3] $\left|\int d\xi\, d\eta\, X(\xi, \eta) Y(\xi, \eta)\right|^2 \leq \left|\int d\xi\, d\eta\, X(\xi, \eta)\right|^2 \left|\int d\xi\, d\eta\, Y(\xi, \eta)\right|^2$

2.6 Techniques of Imaging a Bose-Einstein Condensate

All information acquired in BEC experiments is deduced from images of the atom distribution. The methods to make images of a condensate can be separated into two major categories: destructive (e.g absorption imaging) and non-destructive techniques (e.g. phase contrast imaging). In the first category the BEC is (as the name already suggests) destroyed, while in the second one the condensed state is maintained. Non-destructive methods are mainly used for BEC's with a large number of atoms ($\approx 10^6$), while the absorption imaging method is also applicable for small atom numbers.

2.6.1 Absorption Imaging

The standard technique to image a BEC is the Absorption Imaging method which is also used in our experimental setup. A detailed description of the whole setup can e.g. be found in [29] or [30].

The BEC is illuminated with a resonant collimated beam, thus the atoms absorb photons and re-emit them in a random direction. Consequently, the intensity behind the cloud is reduced according to the density distribution of the atoms. This 'shadow image' is then projected with a lens (system) onto the chip of a CCD camera.

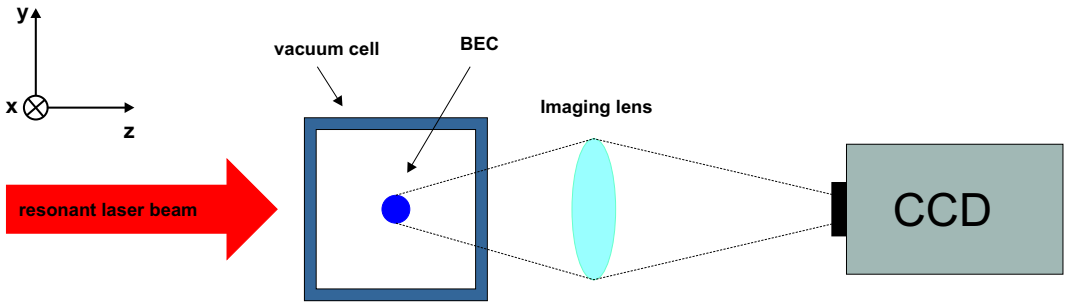

Figure 2.11: Schematic overview over the Absorption Imaging setup. The atomic cloud is illuminated with a resonant laser beam. The atoms absorb the light and re-emit it in a random direction, leading to a decrease in intensity directly behind the cloud. This 'shadow image' is then projected onto a CCD camera, by means of an imaging lens.

This method has a disadvantage: the illumination of the cloud with resonant light leads to a heating up of the atomic sample and therefore to an instantaneous destruction of the condensate. Hence, to observe dynamics a new BEC has to be created for each time step, requiring a stable reproduction of the starting conditions.

In one realization of the experiment three images are taken. The first one includes the atom distribution I_{pic}, the second one is a reference picture I_{ref}, which is taken under the same conditions as the first one but without atoms and the last one is a background picture I_b where all lasers are switched off. The evaluation of the pictures is done in the following steps. First the relative transmission $T(x, y)$ is deduced from all three pictures.

$$T(x,y) = \frac{I_{pic}(x,y) - I_b(x,y)}{I_{ref}x,y - I_b(x,y)} \tag{2.48}$$

The division in (2.48) eliminates all stationary interference fringes which may be caused by the vacuum cell or the imaging optics. From this expression it is then possible to deduce the total number of atoms in the cloud. The laser beam traveling through the cloud along the z-axis corresponds to a projection into the x-y plane on the CCD camera. Therefore, the transmission is only dependent on the column density

$$n_{x,y} = \int dz\, \rho(x,y,z). \tag{2.49}$$

The intensity decrease along the z-axis obeys

$$\frac{dI}{I} = -\rho(z)\sigma(z)dz \tag{2.50}$$

where the scattering cross section is given by

$$\sigma(z) = \frac{\Gamma h\nu}{2I_s} \frac{1}{1 + \left(\frac{I(z)}{I_s}\right) + \left(\frac{2\delta}{\Gamma}\right)^2} \tag{2.51}$$

I_s is the saturation intensity and Γ the line width. In the high intensity limit $I/I_s \gg 1$ and for resonant illumination ($\delta = 0$) equation (2.50) is easy to integrate, yielding for the atom number in a column with base of a pixelsize

$$N_{Pixel} = \frac{A}{M^2} \frac{2I_0}{\Gamma h\nu} \left(1 - T(x,y)\right). \tag{2.52}$$

where A denotes the area of one pixel. It is important to note that the assumption of the high intensity limit leads to an overestimation of the atom number of about 10%. Details can be found in [29].

2.6.2 Dark Field and Phase Contrast Imaging

In this section we want to have a look on two standard non-destructive imaging methods which are based on dispersive effects in the atomic cloud [31]. While propagating through the cloud an off-resonant laser beam experiences a phase shift which is spatially dependent on the atom distribution.

If E_0 is the incident field the field after the cloud becomes $E(x,y) = E_0 \exp(-\mu(x,y) + i\phi(x,y))$, both $\mu(x,y)$ and $\phi(x,y)$ depend on the column density $n(x,y)$ via:

$$\mu(x,y) = k\beta n(x,y) \quad \text{and} \quad \phi(x,y) = k\delta n(x,y) \tag{2.53}$$

The absorption and phase coefficients belong to a complex valued refractive index of the form:

$$n(\mathbf{r}) = 1 + \rho(\mathbf{r})(\delta + i\beta) \tag{2.54}$$

Since most detectors are not phase sensitive, the phase information has to be transferred into intensity. To do so, the fraction of the light scattered by the atoms must be separated from the undisturbed part. Figure 2.12 a) shows a setup solving this problem.

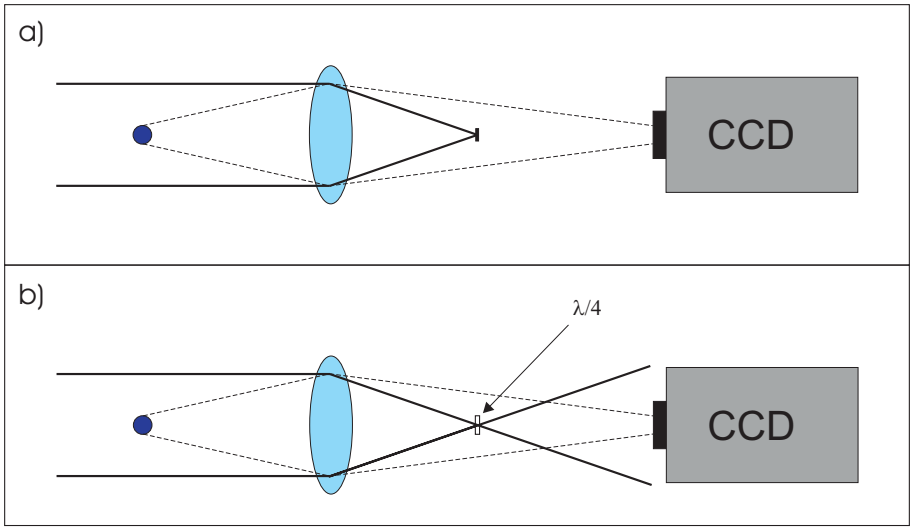

Figure 2.12: a) Dark field imaging setup: The unscattered light is filtered out by a small opaque block b) Similar setup for phase contrast imaging: The fraction of light, not scattered by the atoms suffers a phase shift of $\lambda/4$ and interferes with the scattered fraction on the CCD chip. This method is more sensitive on small phase shifts acquired while passing through the atomic cloud.

The unscattered part of the light is focused in the focal plane of the imaging lens. There it is filtered out by a small opaque block, whose size must be chosen adequate, ideally of focus size, in order not to influence the scattered light too much. Anyway information about small structures is located at the margin of the Fourier plane, hence the size is not that critical. As already mentioned one can write the field after passing through the atoms as the sum of the unscattered fraction E_0 and the part which interacted with the atoms ΔE.

$$E = tE_0 \exp(i\phi) = E_0 + \Delta E \tag{2.55}$$

t accounts for the transmission of the cloud and ϕ is the phase shift suffered by the light. In the dark field imaging method E_0 is blocked, so the intensity detected with the CCD camera is given by

$$
\begin{aligned}
I &= \left|\Delta E^2\right| \\
&= I_0 \left|t \exp(i\phi) - 1\right|^2 \\
&= I_0[1 + t^2 - 2t\cos(\phi)]\,.
\end{aligned}
\tag{2.56}
$$

An expansion of the last line in (2.56) shows that for small ϕ the intensity is quadratically dependent on the phase shift.

The similar setup for phase contrast imaging shows Figure 2.12 b). The only difference is that the unscattered light is not blocked but phase shifted by $\lambda/4$ with a plate of appropriate thickness and made interfere with the scattered field. The intensity incident on the CCD chip can consequently be written as

$$
\begin{aligned}
I &= \left|E_0 \exp(i\frac{\pi}{2}) + \Delta E\right|^2 \\
&= I_0 \left|\exp\left(i\frac{\pi}{2}\right) + t\exp(i\phi) - 1\right|^2 \\
&= I_0 \left|2 + t^2 + 2t\left(\sin(\phi) - \cos(\phi)\right)\right|
\end{aligned}
\tag{2.57}
$$

If one performs again an expansion of the last line in (2.57) one can see that the intensity goes linear for small ϕ. Therefore one can say that phase contrast imaging is more sensitive in the case of small phase shifts.

2.6.3 Diffraction-contrast Imaging

Another minimal destructive method based only on diffraction effects was suggested by *Turner et. al.* [32]. For this method no imaging optics is needed. In principle the object is illuminated with a detuned laser beam and the diffraction pattern at a distance z is recorded with a CCD camera. Restrictions to this method are that the object must not be strongly absorbing and the phase shift experienced by the light field is spatially not too variant

$$
2\mu(x,y) \ll 1 \quad \text{and} \quad \left|\phi(x+a, y+b) - \phi(x-a, y-b)\right| \ll 1. \tag{2.58}
$$

Under these assumption it is possible to derive a relation between the Fourier transforms of the normalized contrast $I/I_0 - 1$ and the column density:

$$
\mathcal{F}\left[\frac{I - I_0}{I_0}\right] = 2k \left(\underbrace{\delta\sin(\pi\lambda z u^2) - \beta\cos(\pi\lambda z u^2)}_{\tilde{h}(u,z)}\right) \mathcal{F}\left[n(x,y)\right] \tag{2.59}
$$

u is the spatial frequency conjugated to the spatial coordinates. $\tilde{h}(u, z)$ is called *Contrast Transfer Function* (CTF). Please do not confuse this function with the *Coherent Transfer Function* defined in subsection 2.4.1. This relation can then be solved for the column density, where some care has to be taken, since the CTF has zeros which makes it an *ill-posed* inverse problem. For a phase delaying object $\delta > 0$ one zero point is located at small spatial frequencies, while for a phase advancing object $\delta < 0$ the first zero occurs for rather high frequencies. Hence, the object should advance the phase in order to make the reconstruction process of the column density more stable. For cold atoms this is possible by using light which is blue detuned from the resonance. Although no lenses are used magnification is also possible by using a point source for illumination instead of a collimated beam. If R_1 is the distance from the point source to the cloud and R_2 is the distance from the cloud to the chip of the CCD camera, the magnification is given by $M = (R_1 + R_2)/R_1$.
Up to now, this method has not been tested for a Bose-Einstein Condensate. The question is, whether the requirements in Equation (2.58) are good assumptions when imaging a BEC. For a minimally destructive method the weak absorption condition is necessarily fulfilled. The slowly varying phase condition is more critical. Objects with a peak phase-shift of order one radian most likely satisfy this condition. When the detuning of the imaging beam amounts $\rho_{max}\sigma_0/4$ full linewidths from the resonance, where ρ_{max} is the maximal column density and σ_0 the resonant cross section, this peak phase-shift is reduced to one radian. An appropriate value is a detuning of 100Γ. The authors predict that for a BEC in a glass cell and $R_1 = 12$ mm and $R_2 = 60$ mm, a resolution of 3.7 μm can be achieved.

3 A New Objective for High Resolution Imaging

This chapter is devoted to the new imaging setup built up during this thesis. First, a motivation will be given, why an extension of our current setup with a high resolution imaging device is necessary. In the next two subsections, the lens system itself and the mount accommodating the lenses are described in more detail. Several test measurements were performed evaluating the imaging power of the system, concerning resolution, field of view, astigmatism as well as the influence of a tilt of the objective with respect to the vacuum glass cell. The resolution was estimated doing a best-fit analysis. The results of this measurement were then confirmed in a more direct way, making use of the so called Talbot effect, which is the generation of self-images of a grating by diffraction at certain distances behind it [33]. The achieved resolution is 1.1 μm, which enables the observation of structures on the scale of the healing length, e.g vortices or dark solitons. The new setup does not only consist of the objective, also the CCD camera with which the images are acquired plays a decisive role. Test measurements concerning noise and quantum efficiency showed that our camera is shot noise limited and has an efficiency of 38%.

3.1 Why a new Objective?

The project was actually started by Jonas Fölling during his diploma thesis [34]. The first motivation for the new objective was the generation of arbitrary potentials by scanning a focused, detuned laser beam over the BEC in a given pattern in a time T of under 1 ms. By varying the pattern over time, time dependent potentials can be created. Clearly, the spatial resolution of the pattern is given by the spot size in the focus. Hence, an objective adapted to our requirements with a high numerical aperture is absolutely necessary. But the implementation of the objective as such a phase imprinting device has not been followed up to now, I rather concentrated on the application of the objective as a high resolution imaging device. Since all data in BEC experiments are deduced from images of the atom distribution, it is important that the quality of the imaging system is as good as possible. A crucial parameter is the so called healing length, which is given by [15, 35]

$$\xi = \sqrt{\frac{\hbar^2}{2mgn}} \tag{3.1}$$

where m is the mass of the particles, g is the coupling constant [1] of the two body interaction and n is the density of the atomic sample. Simply speaking, the healing length is the typical length scale on which the density in a BEC varies. For typical experimental parameters this healing length is in the sub micrometer range, but especially for small condensates it can be tuned to be on the order of one micrometer. Therefore a resolution in this regime is desirable. This would make it possible to observe many effects directly as e.g. the generation of vortex pairs in the Berezinskii-Kosterlitz-Thouless crossover [36] or the creation of dark soliton fans [37, 38, 39]. In both cases a knot in the wave function appears. Since the density increases on the order of the healing length these structures could be seen with an adequate imaging system. Another possible application is the measurement of density fluctuations in a Bose gas [40].

3.2 Lens Data

The new objective consists of three lenses made of SF11 glass coated with an antireflection coating with a central wavelength of 780 nm. The design of the lenses, including the numerical calculations of the shape and the relative position of the lenses have been accomplished by *Carl Zeiss Laser Systems*. Details of the single lenses and of their objective configuration are shown in Figure 3.1. Several restrictions have to be fulfilled by the objective. The diameter of the objective including the lens mount must not exceed 34 mm since the access to the vacuum glass is limited by a circular aperture of ≈ 35 mm, belonging to the mount of the B-field coils. If the objective is used as a phase imprinting tool, the focal length must be big enough so that the focus is at the atom's position within the glass cell. The glass cell has a side length of 38 mm including the walls with a thickness of 4 mm. So the focus must be 22 mm away from the front end of the objective, when two millimeters play between the objective and the glass cell are desired. Additionally, the optical properties of the glass cell have to be taken into account when designing the lenses. The cell consists of quartz glass and the refractive index was assumed to be 1.458.

3.3 Lens Mount

A mount for the lenses was not available from *Carl Zeiss Laser Technik*, therefore a suitable housing was designed and machined in the workshop of the institute. Figure 3.2 shows a cut through the complete objective. The objective mount consists of two parts made of brass. A technical drawing of the first one is shown in the Appendix in Figure A.2. The lenses lie on the knife edges which are drawn in detail also in this figure. This way of mounting is necessary as the lenses have a bevel on their outer rim being too coarse to mount the lenses without tilt to each other. With the help of the knife edges the lenses bear on their polished surface avoiding an angle between the lenses. The fetch

[1] The coupling constant g itself depends on the s-wave scattering length a via $g = 4\pi\hbar^2 a/m$.

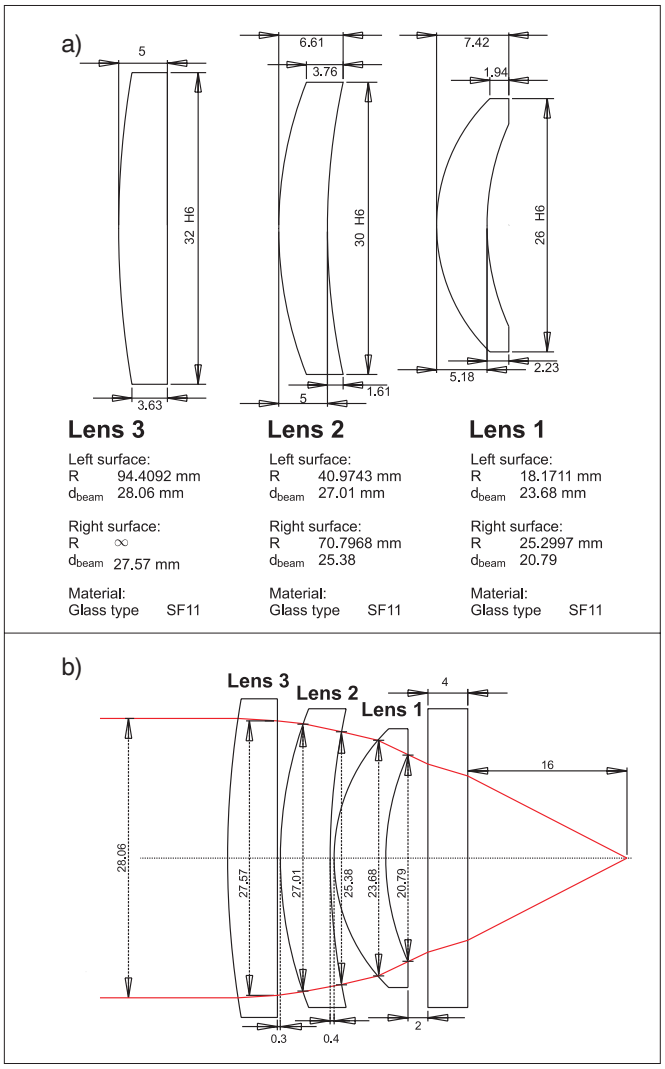

Figure 3.1: a) Technical data of the single lenses b) Lenses in their objective configuration with beam path for focusing a collimated beam

between the lenses and the housing is 15 μm according to the H6 DIN standard. This part of the lens mount was milled in one clamping, in order to reach a nice centering of both lenses. At the position of the second lens, the mount was machined so precisely that no fixing of the lens is necessary. The friction between lens and housing is sufficient to keep the lens at its designated position. Lens three is clamped into the objective by means of a plastic tube and a retaining ring screwed at the back end of the objective. Lens one is mounted in a separate component, which is screwed into the first part via a fine thread with a pitch of 0.35 mm. An O-ring is pressed between the two components so that the play of the thread is minimized. Figure 3.3 gives an overview over this part of the mount. The thread enables fine tuning of the position of the first lens. It turned out that the imaging quality is best when this part is screwed into part one as far as possible.

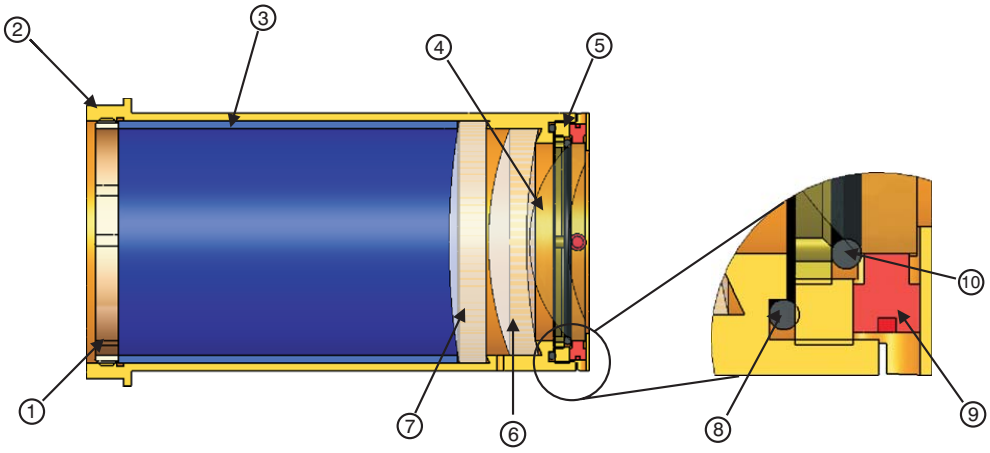

Figure 3.2: Cut through the complete objective mount with lenses. (1) retaining ring for the plastic tube, (2) first part of the housing, (3) plastic tube for fixing lens three, (4) Lens one, (5) retaining ring for lens one, (6) lens two, (7) lens three, (8) first O-ring, (9) adjustment screws, (10) second O-ring

Lateral fine tuning of the first lens is also possible by means of four adjustments screws. This was actually recommended by *Carl Zeiss Laser Systems* but emerged not to be necessary within the possible fetch of 0.1 mm. A lateral displacement does not influence the imaging properties significantly. To be sure that the lens lies flatly on its bearing

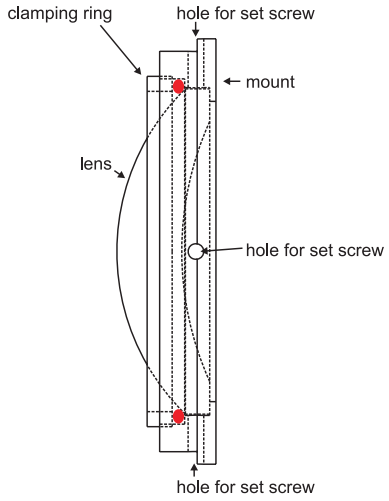

Figure 3.3: Mounting component for the first lens

plane, an O-ring is pressed on the lens with the help of a clamping ring. In Figure 3.3 the O-ring is indicated as a red circle. The technical drawings of all components of the objective are given in Appendix A.

3.4 Test Measurements

Before installing the objective into the experimental setup a thorough analysis of its imaging properties has to be done. The test measurements include tests concerning magnification, resolution and field of view. Additionally, it was estimated how the imaging quality is changed by a possible tilt of the objective with respect to the vacuum glass cell in the experiment. All measurements have been performed with the same components which will be installed in the experiment with exception of the vacuum cell. To simulate the influence of the cell I used a glass plate made of the same material and the same thickness as the wall of the cell. For performing the test measurements it is necessary to choose an appropriate object for imaging with the objective. Especially for the evaluation of the resolution it is essential that the structures on the test target are smaller or at least comparable to the expected value of the resolution. In our case the expected value is on the order of 1 μm and so a gold grating consisting of holes with a diameter of 650 nm and a relative distance of 20 μm was taken. The measurement of the magnification was done with a standard objective micrometer scale as described later.

3.4.1 Test Setup

A schematic overview over the test setup is shown in Figure 3.4:

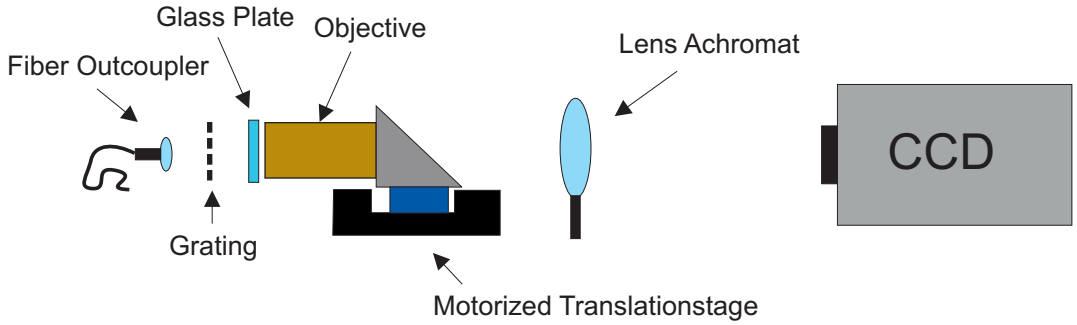

Figure 3.4: Setup for testing the imaging properties of the objective: The grating is illuminated by a laser beam from behind and is placed in the focus of the objective, leading to a projection to infinity. The backtransformation is done with an additional achromatic lens that projects the image onto the chip of a CCD camera. The glass plate is used for the simulation of the ultra high vacuum cell in the actual experimental setup.

In principle imaging with the objective works as follows: The test object is placed in the focus of the objective with the glass plate in between. So the objective performs a transformation of the object to infinity, while the backtransformation is done with an additional achromatic lens *(Melles Griot LAO 677, focal length = 350 mm)*. The reason why it is done in this way is easy to understand. As already mentioned, the objective was designed for focusing a collimated beam with a flat wavefront. Exactly the same

happens while imaging a point-like object with the method described above, just the other way round. The objective transfers the spherical wavefront emerging from the object into a flat one. When using the objective alone, the outgoing wavefront must also be of spherical shape, but this will happen with a bigger amount of spherical aberration, and there will be more light in the maxima of higher order in the PSF.
The distance of the achromat to the CCD-Camera *(QImaging Retiga Exi)* must equate its focal length. To fix this distance a collimated beam with a wavelength of 780 nm and a waist of 2.54 mm was focused on the camera by moving the lens with the help of a manual translation stage and recording the waist of the fitted gaussian as a function of position.
Illumination of test object was done with the same laser beam from behind. The distance to the glass plate was 16 mm, which is approximately the distance of the atoms to the wall of the vacuum cell in the actual experiment. The plate was fixed on a prism mount in order to be able to tilt it with respect to the objective, which was mounted with the help of an angle bracket on a motorized translation stage *(Physical Instruments PI M111 2DG)* and could be moved with a precision of 0.2 μm. Traveling distances are measured in encoder counts, where 1000 counts correspond to (8.58 ± 0.02) μm. This allowed to move the objective until a sharp image of the object was reached.

3.4.2 Magnification

The first measurement concerned the magnification, since this is a necessary factor for evaluating the resolution. As test object a standard objective micrometer scale was taken, since rather big structures are favourable for this measurement. The spacing of the lines is 10 μm. The cut through the image was taken in a region where the spacing

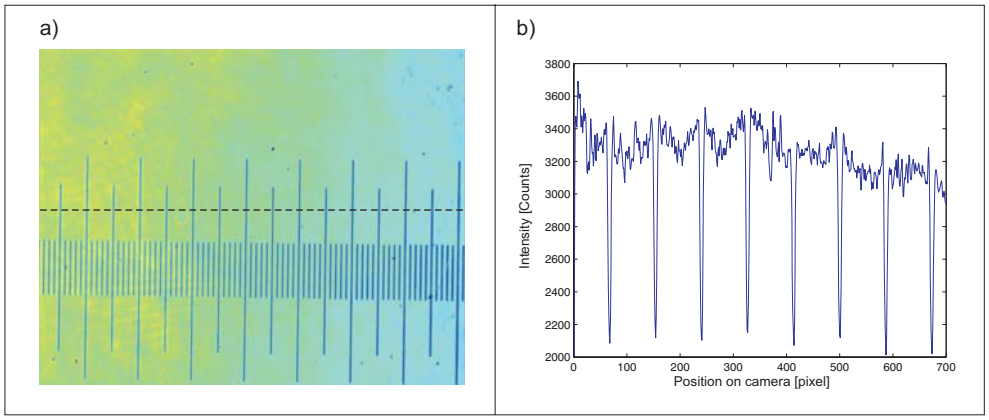

Figure 3.5: a) Image of the objective micrometer scale acquired with the setup described above. The line spacing is 10 μm. As the pixelsize is known the magnification can be derived from this picture b) Cut through the image along the dashed line shown in a)

of the lines is 50 μm. Comparing this to the spacing in pixels on the camera and taking into account the pixelsize of 6.45×6.45 μm^2 yields a magnification of 11.18 ± 0.03. The

slight tilt of the micrometer scale was also considered. Theoretically the magnification is given by:

$$M = \frac{f_{Obj}}{f_{Achr}} \tag{3.2}$$

where f_{Obj} and f_{Achr} are the focal lengths of the objective and the achromatic lens respectively. Inserting $f_{Obj} = 31.23$ mm and $f_{Achr} = 350$ mm in (3.2) results in a theoretical magnification of 11.2, which is in very good agreement with the experimental value.

3.4.3 Resolution

Resolution is a crucial feature of an imaging system, since it describes the ability to reproduce fine structures of the sample in the imaging plane. It is commonly defined as the minimum distance of two points at which they are still distinguishable in the image. As described in section 2.3 the resolution is according to the Rayleigh criterion given as the distance between the central maximum and the first minimum of an Airy function. It is directly connected to the numerical aperture NA of the objective via [27]:

$$\Delta r = 0.61 \frac{\lambda}{NA} \tag{3.3}$$

The numerical aperture of our objective is specified as 0.45. Substituting this and the used wavelength of $\lambda = 780$ nm in (3.3) gives a theoretically expected value for the resolution of 1.1 μm.

A standard method to measure the resolution of an imaging system is to image a very small, point-like object, whose size is smaller than the expected value of the resolution. With this method the PSF of the imaging system is directly recordable. For estimating the resolution of our objective a gold grating consisting of holes with a diameter of 650 nm and a relative distance of 20 μm was used. A scanning electron microscope (SEM)

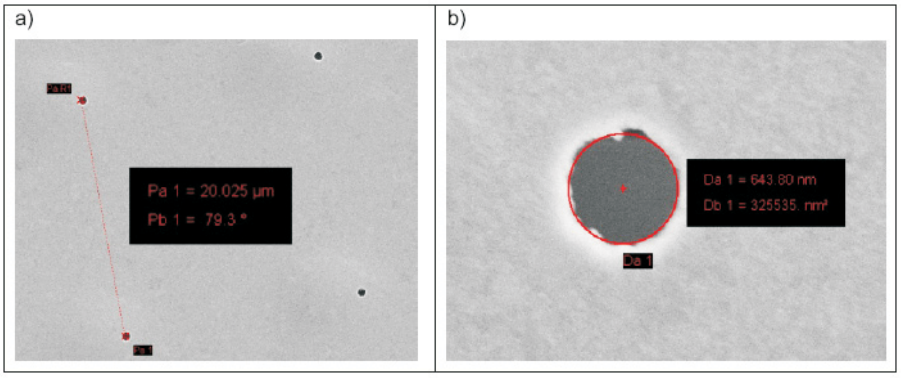

Figure 3.6: a) SEM micrograph overview over a region including four holes on the gold grating, the holes are separated by 20 μm b) Picture of a single hole with a diameter of $\approx$ 650 nm.

micrograph of the grating is shown in Figure 3.6. These pictures have been done by Martina Schürmann from the Institute of Physical Chemistry.

For determining the resolution one of the holes was chosen and the objective was focused on it. The focusing procedure was done in the following way: The objective was moved with respect to the grating in equally spaced steps, took pictures at each position and fitted gaussian functions to the acquired intensity profile. The position of the focus is then given as the position with the smallest waist. The result of such a measurement can be seen in Figure 3.7 (see also section 3.4.5). From this figure it is also possible to deduce the depth of field of the imaging setup. It is defined as twice the range in which the fitted waist increases by a factor of $\sqrt{2}$. I get a value of about 6.8 μm.

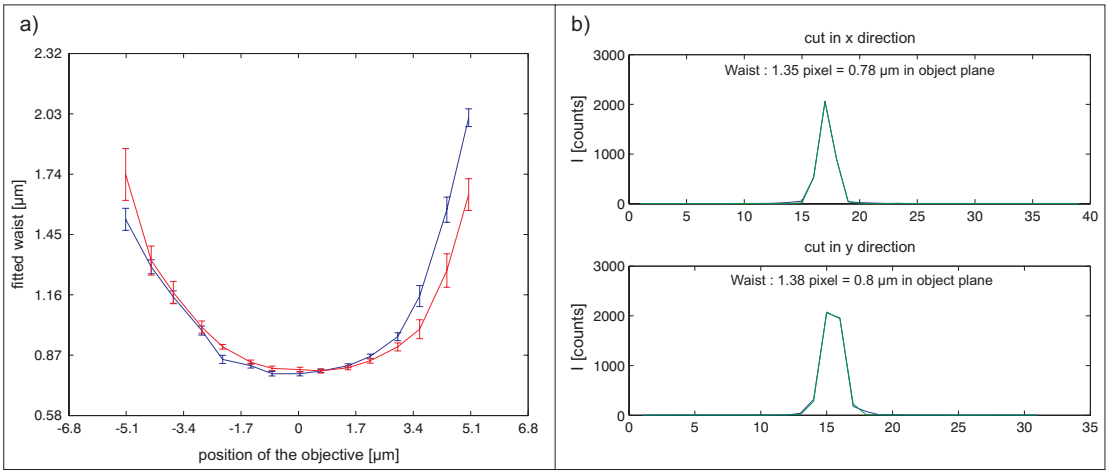

Figure 3.7: a) Width of the gaussian fits to the intensity distribution of a single hole vs. position of the objective. The blue curve denotes the waist in x direction, while the red curve represents the y direction. b) Typical cuts through the picture in x and y direction and their gaussian fits in the focus.

The resolution was estimated doing a 2-d best fit analysis. The idea is to compare the real image with the result of simulations. An overview over the fitting procedure is shown in Figure 3.8 a). First of all the hole is approximated by a circle with a diameter of 650 nm. For simulating the imaging process I assume a PSF of the following form [2] (see section 2.3)

$$\mathrm{PSF}(r) = \frac{2\, J_1\left(\frac{1.22\pi}{\Delta r} r\right)}{\frac{1.22\pi}{\Delta r} r} \tag{3.4}$$

where Δr denotes the resolution according to the Rayleigh criterion and J_1 is the Bessel function of first kind. The imaging is simulated by convolving the circle with the PSF given above, and taking its absolute square. The absolute square is taken afterwards, as

[2] Strictly speaking, this PSF is only correct when the imaging system is diffraction limited, but we will see that in our case this leads to a good agreement between experiment and simulation.

in the experiment the illumination of the sample is done with a coherent laser beam (see sections 2.4.1 and 2.4.2). In order to keep the numerical error small, the convolution is done on a grating whose pixelsize is twelve times smaller than the pixels of the camera. This is taken into account by covering the result of the convolution with a grating ('pixel grating' in the flow chart) whose pixelsize is the same as in the experimentally acquired picture and summing over the pixels of this coarser grating.
There are two free parameters for the fit: on the one hand the position of the 'pixel grating' and on the other hand the resolution of the PSF. During the fitting procedure the 'pixel grating' is first moved to a certain position and then the convolution is done for different resolutions varying between $\Delta r = 0.3$ μm and $\Delta r = 3$ μm in steps of 0.1 μm. The RMS deviation from the experimentally taken image is computed in each step, but only the smallest value is saved together with the position of the grating. Part b) of Figure 3.8 shows the minimal RMS deviation in dependence of the position of the grating[3]. From this graph the optimal position of the grating can be deduced. In part c) the RMS deviation for this optimal position, but different values for the

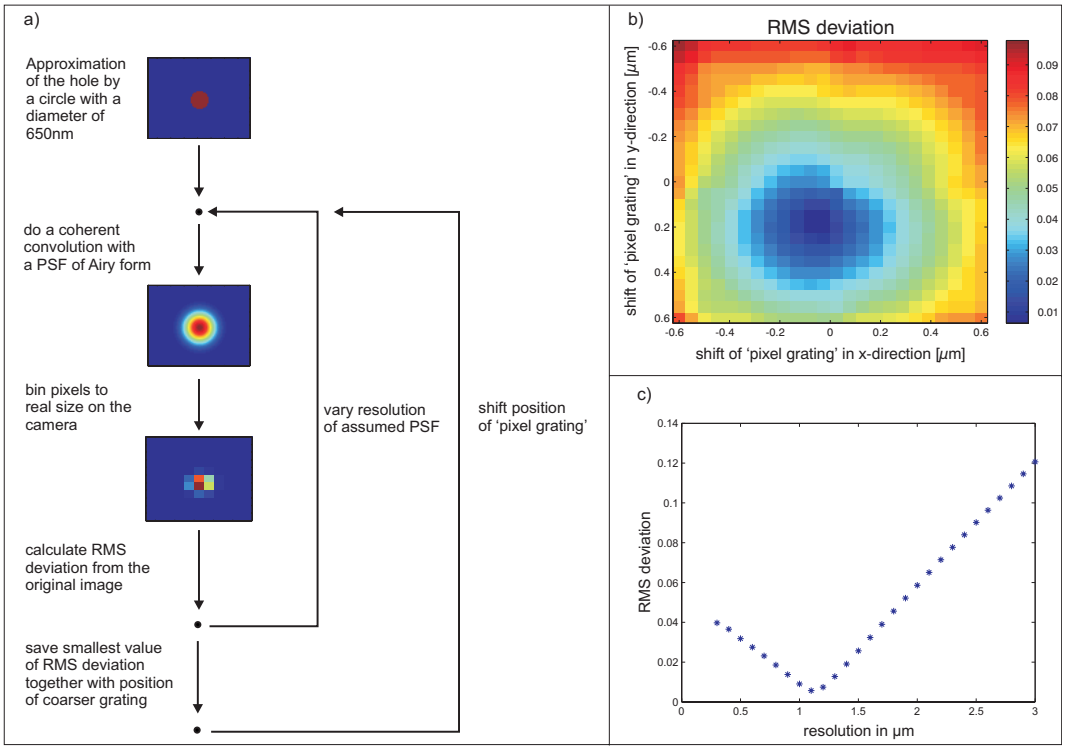

Figure 3.8: a) Schematic overview over the fitting procedure b) Minimal RMS deviation for different positions of the 'pixel grating'. c) RMS deviation vs. resolution for the best position of the 'pixel grating', The graph shows a clear minimum at a resolution of 1.1 μm.

[3]One may expect in this figure a periodicity on the size of one pixel of the 'pixel grating', as the resultant pattern should be the same when the grating is shifted by one whole pixel. This is actually true and was also checked, but the pattern is then shifted with respect to the real image. Hence, there is only one optimal position.

resolution is shown. The graph shows a clear minimum at $\Delta r = 1.1$ μm according to the Rayleigh criterion which is in very good agreement with the theoretical value. The error is estimated by performing the fitting procedure for different pictures of the hole which yields an uncertainty of 0.1 μm. So the resolution of this new imaging setup is assumed to be 1.1(1) μm. In Figure 3.9 a picture of the hole, the best fit and cuts through both are given, yielding a good agreement. This is one of the main results of the thesis at hand, as it means the realization of a diffraction limited imaging system with high resolution, opening up new avenues in the field of cold atoms.

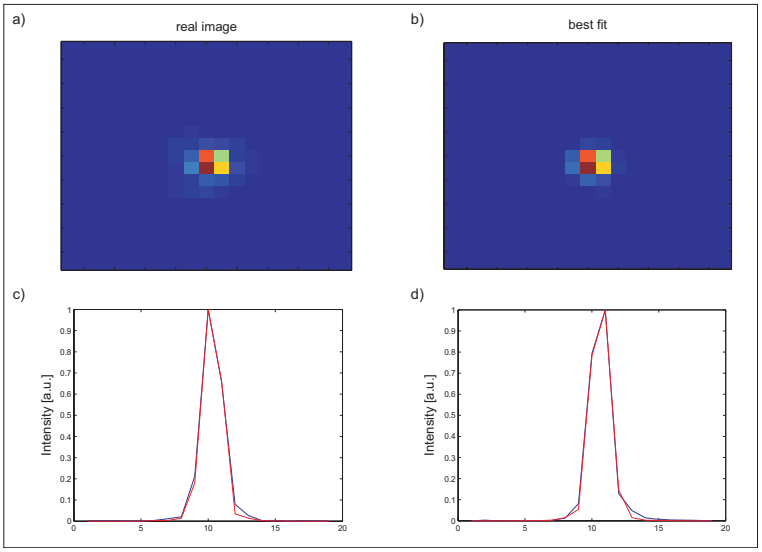

Figure 3.9: a) Real picture of the hole b) Best fit acquired with the method described above c) Cut in x direction through maximum d) Cut in y direction through maximum. In c) and d) the blue curve depicts the cut through the real and the red one through the simulated picture. The agreement is good.

3.4.4 Talbot Effect

When thinking about diffraction, what usually comes to your mind are far-field effects, as for example the diffraction pattern in the double slit experiment. The effects in the near field are often not so familiar. One of these effects is the Talbot effect, which occurs when a grating is illuminated with a plane coherent wave. The grating will reconstruct itself after the so called Talbot distance T_l depending on the used wavelength λ and the grating constant d

$$T_l = \frac{2d^2}{\lambda}. \tag{3.5}$$

This can be understood by application of the Fresnel diffraction formula (2.7). For simplicity, we restrict ourselves to the one dimensional formulation, but there is no

problem to transfer the formulas to two dimensions. Let $T(x)$ be the transmission function of the grating, the field distribution after the distance z is then given by

$$U(x', z) = \frac{\exp(ikz)}{i\lambda z} \int dx\, T(x) \exp\left[i\frac{\pi}{\lambda z}(x - x')^2\right]. \tag{3.6}$$

Since $T(x)$ is a periodic function in x, one can expand it in a Fourier series [41]

$$T(x) = \sum_j T_j e^{ijk_x x} \tag{3.7}$$

with $k_x = \frac{2\pi}{d}$. Inserting (3.7) in (3.6) and sorting the terms yields

$$U(x', z) = \frac{\exp\left[i\left(kz + \frac{\pi}{\lambda z}x'^2\right)\right]}{i\lambda z} \sum_j T_j \int dx \exp\left\{i\left[\frac{\pi}{\lambda z}x^2 - x\left(\frac{2\pi}{\lambda z}x' - k_x j\right)\right]\right\} \tag{3.8}$$

evaluation of the integral [42] results in

$$U(x', z) \propto \sum_j T_j \exp\left(-i\pi\lambda\frac{j^2}{d^2}z\right) \exp\left(ijk_x x'\right). \tag{3.9}$$

From this equation one can derive the Talbot condition. Whenever

$$z = 2m\frac{d^2}{\lambda} \quad m \in \mathbb{Z}^+ \tag{3.10}$$

the field distribution is proportional to the Fourier expansion of the transmission function and therefore the diffraction pattern is a reconstruction of the grating itself. At distances of $z = (2m + 1)\frac{d^2}{\lambda}$ also self-images can be found, but they are shifted in x-direction by half a period.

This effect was also demonstrated with the test setup for the new objective and the same grating as I used for the determination of the resolution (see Figure 3.10). The grating constant was $d = 20$ μm and the wavelength of the illuminating laser $\lambda = 780$ nm. This accounts for a Talbot length of 1025 μm. The first reproduction of the grating was found at a distance of (513 ± 4) μm, which corresponds to the first shifted self-image. The second self-image was found at a distance of 1028 ± 4 μm, what is in good agreement with the theoretical value.

At distances which are a fraction of half the Talbot distance also grating structures are produced but with another period. At a distance of

$$z = \frac{1}{n}\frac{d^2}{\lambda} \quad n \in \mathbb{Z}^+ \tag{3.11}$$

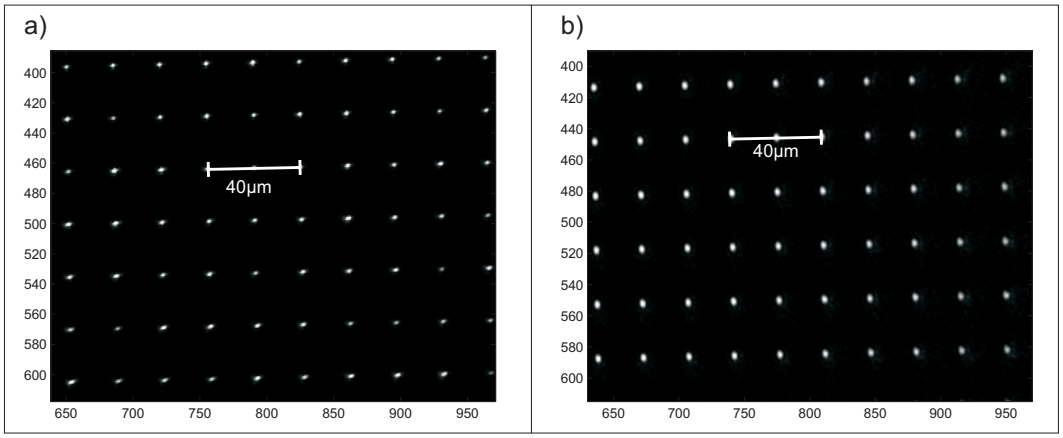

Figure 3.10: a) Picture of the grating b) Picture of the intensity distribution at a distance of half the Talbot length after the grating. The grating is reproduced but with a shift of half a period.

the grating constant amounts

$$d' = \frac{1}{n}d. \tag{3.12}$$

Theses patterns are composed of n real Talbot images, which are laterally shifted by the fraction $1/n$ of the grating constant [43, 44].

This is understandable by inserting (3.11) into (3.9). It follows

$$U(x', \frac{1}{n}\frac{d^2}{\lambda}) \propto \sum_j T_j \exp\left(-\frac{\pi i}{n} j^2\right) \exp(ijk_x x'). \tag{3.13}$$

The summation index j is rewritten as $j = rn + s$ and the summations over r and s are splitted

$$U(x', \frac{1}{n}\frac{d^2}{\lambda}) \propto \sum_{s=1}^{n} \exp\left(-\frac{\pi i}{n} s^2\right) \sum_{r=-\infty}^{\infty} T_{rn+s} \exp\left(\frac{i\pi}{d}(rn+s)x'\right). \tag{3.14}$$

The substitution of T_{rn+s} by its integral expression and some algebra yield our final result

$$U(x', \frac{1}{n}\frac{d^2}{\lambda}) \propto \sum_{r=1}^{n} T\left(x' - \frac{d}{n}r\right) \underbrace{\frac{1}{n}\sum_{s=1}^{n} \exp\left[\frac{\pi i}{n}\left(s^2 + sr\right)\right]}_{=C(r,n)} \tag{3.15}$$

The constants $C(r, n)$ are called *Talbot coefficients*. This expression clearly shows that the interference pattern at the distance $z = \frac{1}{n}\frac{d^2}{\lambda}$ consists of n copies of the grating shifted by d/n with respect to each other. In Figure 3.11 different experimentally acquired intensity distributions at a fraction of the Talbot length behind the grating are shown.

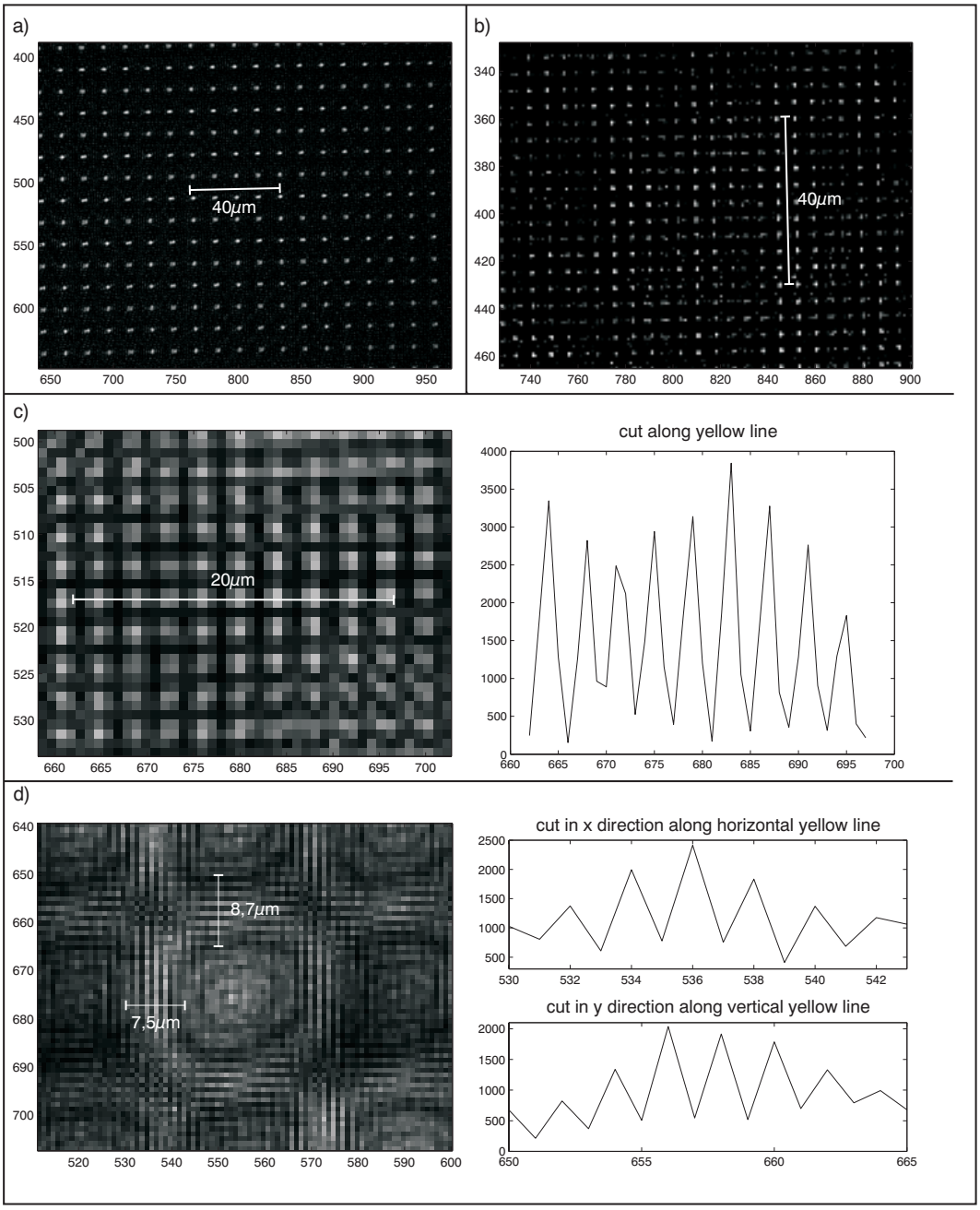

Figure 3.11: a) Image of the intensity distribution at a distance of $T_l/4$ after the grating. The period of the grating is diminished by a factor of two. b) Diffraction pattern at $z = T_l/10$. The period is a factor of five smaller than on the original grating and amounts 4 μm c) $z = T_l/20$ a grating structure is still clearly visible. On the right hand side a cut through the image along the white line is shown. The maxima are equally spaced at a distance of four pixels corresponding to 2.3 μm. Taking the pixelsize into account this is in good agreement with the theoretical value of 2 μm. d) $z = T_l/40$: At this distance from the grating the period of the diffraction pattern should be 1 μm. Although the image is blurred due to the finite depth of field of the objective, a modulation on the length scale of one pixel is obvious, confirming the resolution determined in the last chapter.

Part a) and b) depict the images at 1/4 T_l and 1/10 T_l respectively. As expected the grating constant amounts 10 and $4\mu m$. Also at $z = T_l/20$ a grating structure is still visible as shown in c). The right hand graph is a cut through the image along the yellow line. The intensity maxima are equally spaced by 4 pixels, corresponding to 2.3 μm. The theoretical value is 2 μ m. When considering the pixelsize of 0.58 μm this is in good agreement. Part d) is an image of the interference pattern at a distance of $T_l/40$ behind the grating. The period of the grating given by theory amounts 1 μm. Although the structures are blurred due to the finite depth of field of the objective still a modulation on the one pixel scale is visible, as the cuts clearly reveal. This is a confirmation of the resolution measurement in the last section, since two points separated by approximately one micrometer are still distinguishable. In fact, this is the best result that can be reached, as the limiting factor is now the pixelsize of the camera and not the imaging optics.

3.4.5 Astigmatism

As discussed in subsection 3.4.3 the focusing of the objective was done by fitting a gaussian envelope to the intensity profile of a single hole in dependence of the position of the objective. The focus is then given by the position where the waist in x and y direction are smallest. Figure 3.7 shows a result of such a measurement. The dependence of the waist in x and y direction is quite symmetric having both their minimum at the same point. This is the ideal case, but is not true anymore when astigmatism plays a role. Then the positions of the minima are shifted with respect to each other, the worse the amount of aberration the bigger this astigmatic difference (see section 2.5). Also our

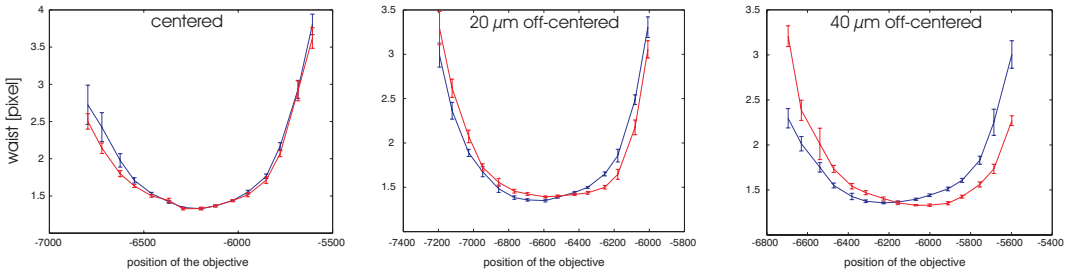

Figure 3.12: Scan through the focus for different holes. On the y-axis the fitted waist is plotted in μm. The blue curve denotes the waist in x-direction, while the red curve represents the y-direction. The left handed graph corresponds to a hole centered on the optical axis. The middle one and the right one are displaced 20 μm and 40 μm respectively.

new imaging setup turned out to suffer from astigmatism for objects not placed on the optical axis. To test this, such scans were also performed with holes neighbouring the one where the scan is symmetric. Figure 3.12 shows scans through the focus for different holes. The error bars are statistical errors. During the measurement ten pictures of the hole are made before the objective moves to the next position. One can see that already

a shift of 20 μm away from the optical axis involves a splitting of the focus in x and y direction what is an indication for astigmatism. With the test setup described above it was not possible to improve this result. After building up the test setup the first time absolutely no symmetric scans had been possible, only after a realignment of the imaging lens the results shown above could be achieved. This leads us to the assumption, that the position of this lens with respect to the objective is rather critical. Hence, in the final setup both the objective and the additional lens should be mounted together in one part, ideally machined in one clamping so that a nice centering of both parts is guaranteed.

3.4.6 Field of View

An important feature of an imaging system is also the field of view. This is the region around the optical axis in the object plane, in which a sharp picture of the object is acquired. The field of view of our objective was estimated by analysing an image of the

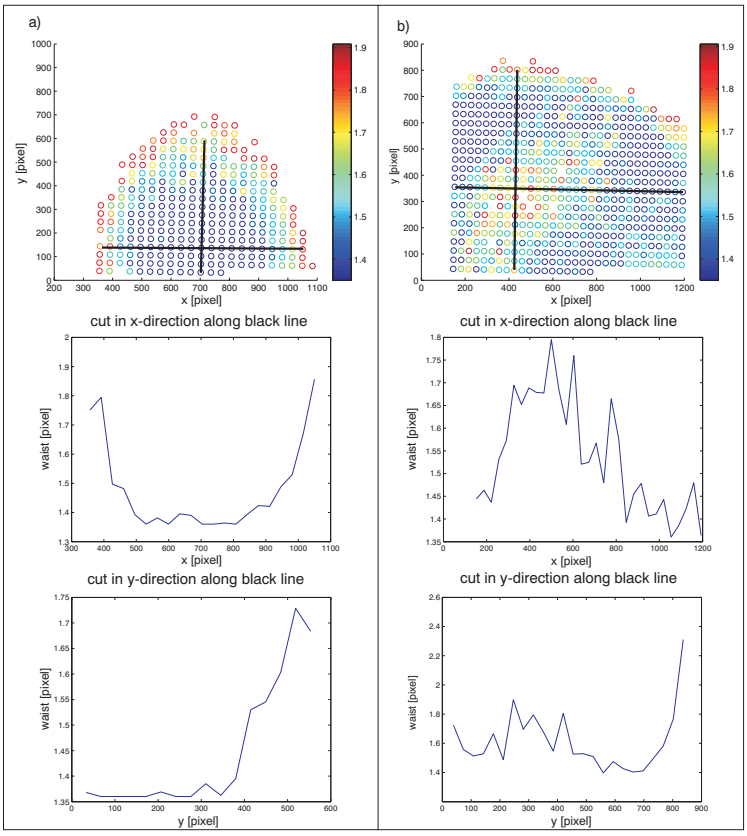

Figure 3.13: For estimating the field of view a picture of the whole grating was taken, and gaussian envelopes were fitted to each hole a) Waist of the gaussian envelope in x-direction measured in pixels, for the region in which the waist increases from its minimum value by a factor of $\sqrt{2}$. Below, cuts along the black lines are shown b) Same for the y-direction. One pixel corresponds to 0.58 μm

whole grating, the same that was used for the estimation of the resolution. To do this, a gaussian envelope was fitted to the intensity profile in each lattice site. In many cases the criteria for the field of view are rather subjective. Here it is defined as the region in which the fitted waist increases from its minimum value by a factor of $\sqrt{2}$. In Figure 3.13 a) each circle stands for one hole of the grating. The color denotes the fitted waist in pixels in x-direction for this region. Below, cuts along the black lines are shown. It is possible to delimit a clear area in which the picture is sharp in the sense given above. In part b) the same is shown for the y-direction. Here it is not possible to find such an area. This is due to the astigmatism described in the last subsection. One can not find a clear focus where the imaging is sharp in both directions except for one point on the optical axis. From this picture it is not possible to deduce the field of view. It must be mentioned that due to this imaging error a gaussian envelope in y-direction is not a good model. Therefore this measurement can only give a rough estimation relying on the results of the fit in x-direction yielding a value of about 400 μm in the object plane. This shows again that great care has to be taken when installing the objective in the setup, especially for the centering of the objective and the additional imaging lens.

3.4.7 Tilt of the Glass Plate

As already mentioned in the theory part, astigmatism is also introduced by imaging through a tilted glass plate (see Figure 2.10). Since all of our experiments are performed in an ultra high vacuum cell made of quartz glass, it is necessary to get an idea about what happens when the objective is tilted with respect to the surface of the cell. This

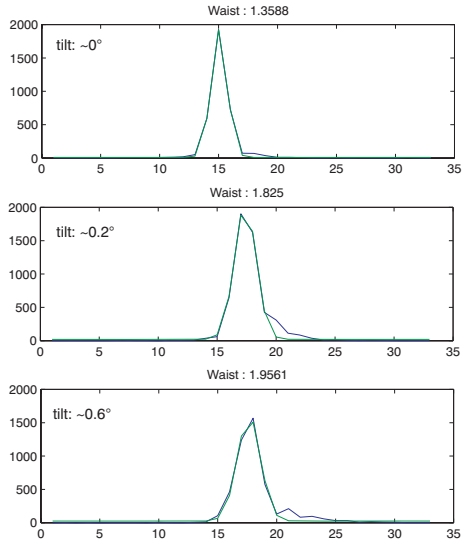

Figure 3.14: The influence of a tilt between objective and the vacuum glass cell was studied by tilting the glass plate in the test setup. The graph shows cuts through the image of a single hole and their gaussian fits for different tilt angles. Already at an angle of 0.2 degrees a tail is clearly visible.

was simulated by tilting the glass plate in the test setup described in section 3.4.1. Therefore the plate was mounted on a standard kinematic prism mount, to allow for a tilt in both directions. Since the pitch of the adjustment screws was known, it was easy to convert turns into a tilt angle. Figure 3.14 shows cuts through images of one hole of the grating for different tilts of the glass plate. While the cut is quite symmetric for a well aligned plate, a tail appears when the plate is tilted. This tail is already clearly apparent for a tilt of 0.2 degrees and enhances for bigger angles. From this we learn that in the final setup a possibility to align the objective parallel to the surface of the vacuum cell must be implemented.

3.5 Installing the Objective in the Experimental Setup

The new imaging system has not yet been installed into the experimental setup, so only a suggestion for the installation can be given. As already mentioned great care has to be taken that the additional imaging lens is as good as possible centered with respect to the objective. Ideally the objective, the imaging lens and the camera are fixed on one part, that can be tilted and moved as a whole. A possible solution is shown in Figure 3.15. All three parts are fixed to a tube with a length of approximately 35 cm. This tube is mounted on a tilting stage, which itself is attached to a two axis translation stage with a clearance hole of 57 mm (*Newport M-406*). Since no tilting stages fulfilling our requirements are available from commercial manufacturers this part will be machined in the workshop of the institute. In the upper part the diameter of the tube is restricted by the clearance hole of the stages. Actually, the tube should be smaller in order to have enough play for alignment of the vertical position and the angle with respect to the glass cell. Below the stages, the diameter of the tube must be bigger and must contain clearance holes, so that there is enough space for the MOT-Optics (see below). The whole construction is carried by an angle bracket screwed onto a motorized translation stage (*Micos LS110*). This translation stage can bear up to 8 kg in the vertical direction and a torque of 30 Nm which is sufficient for our needs. The use of a motorized translation stage is advisable as a fast realignment of the imaging is possible when time-of flight pictures want to be taken.
As the distance between objective and glass cell is only 2 mm the MOT beam coming from above must pass the lens system. In order to get a collimated beam additional optics is needed. In Figure 3.16 a possible lens configuration and the resultant beam path is shown. The incoming beam is first widened up by means of a plano-convex lens and then focused with a bi-convex lens into the back-focal plane of the objective. This results in a collimated beam with a maximum diameter of 2 cm which is restricted by the aperture of the objective. For taking images of the atom distribution in the glass cell, the space between the additional imaging lens and the camera must be free. Therefore, the MOT optics must be removed during one cycle of the experiment. The time between the MOT phase and taking the images is more than half a minute. Hence, it is possible to move these parts out of the beam path with a second motorized translation stage (*Micos VT-80*).

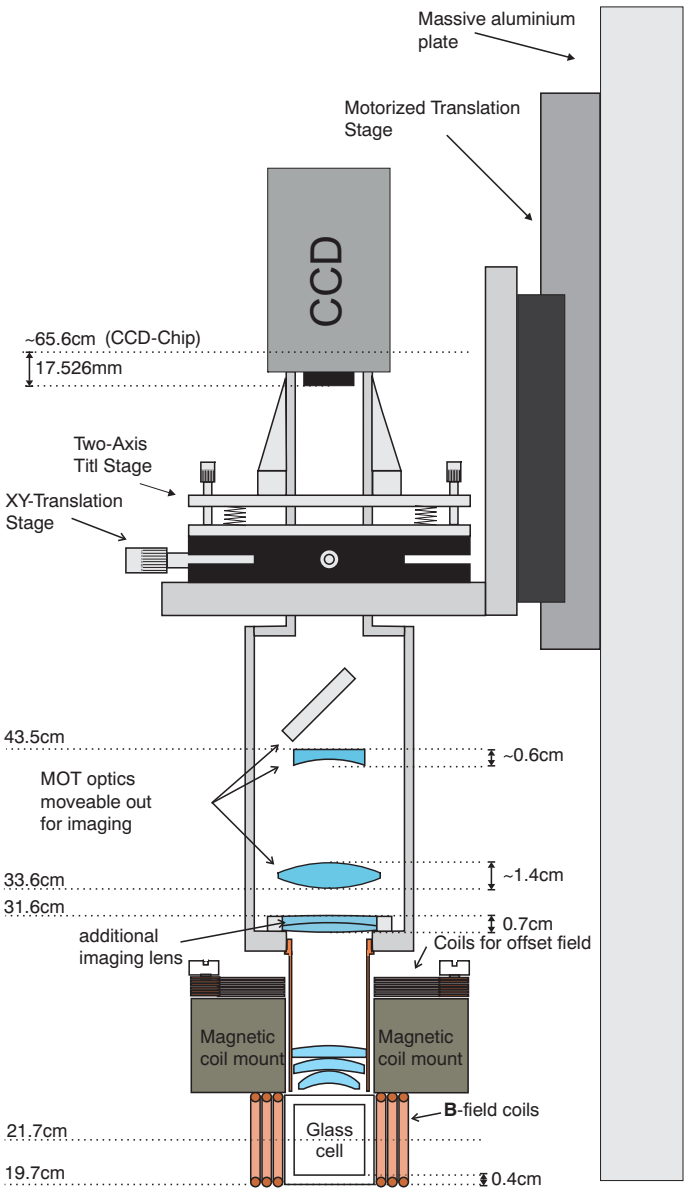

Figure 3.15: Sketch of a possible way of mounting the objective in the experiment. The mechanics for moving out the MOT optics is not shown.

The distance between the additional imaging lens and the chip of the camera must be 340.23 ± 0.15 mm (measured from the lens' surface). According to numerical simulations the resolution is 1.1 μm in this range. The distance of the imaging lens with respect to the objective is not that critical as the beam leaving the objective is collimated anyway. As the distance between the glass cell and the objective is only 2 mm, a collision should be mechanically impossible. The ideal case would be that the lowest position of the motor stage is well above the cell, or a stop should be implemented preventing a crash. This could be realized with a horizontal aluminum plate just below the angle bracket.

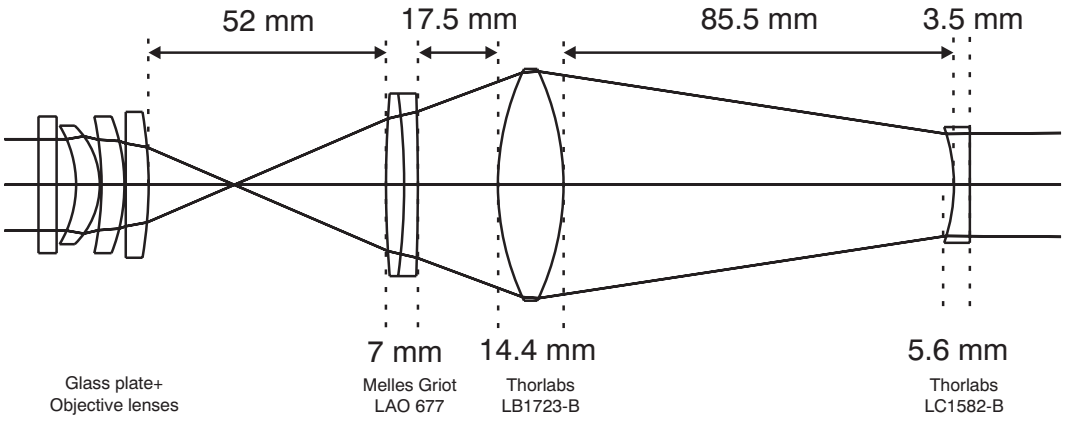

Figure 3.16: The distance between objective and the vacuum glass cell is only 2 mm, so the MOT beam coming from above must pass the objective. In order to get a collimated beam additional optics is needed. The lens configuration shown in this figure results in a collimated beam with a diameter of 2 cm restricted by the front aperture of the objective.

3.6 Characterization of the CCD Camera

For an imaging setup not only the optical components decide on its behaviour but also the detector with which the images are taken plays a significant role. In our case the detector is a CCD camera *(QImaging Retiga Exi)*. Some Specifications given by the manufacturer can be found in table 3.1.

Chip Size	1392×1040 pixels
Pixel Size	6.45×6.45 μm^2
Exposure Control	10 μs to 10.9 min in 1 μs increments
Sensor Type	Sony© ICX285 progressive-scan interline CCD (monochrome)
Digital Output	12 bits
Readout Frequency	$2.5, 5, 10, 20$ MHz
Frame Rate	10 fps

Table 3.1: Camera specifications given by the manufacturer

Two tests have been performed with this camera. The first one concerning noise and gain of the camera, the second one the quantum efficiency.

3.6.1 Noise and Gain

Very important for the quality of a CCD camera is to what extend the acquired images are blurred by noise. Noise sources in the image are readout noise of the camera's electronic, thermal noise and the photon noise itself. The last source is inherent to the particle character of photons. The probability to detect a certain number of photons in a given time interval follows Poissonian statistics. If the mean number of photons

amounts N the standard deviation of the photon distribution will be $\sqrt{N}$. The signal to noise ration (SNR) is therefore $\sqrt{N}$ and increases with increasing photon number, while the other two noise sources are not dependent on the signal. Thermal Noise is caused by noise in the dark current. Even when there is no light on the CCD chip some electrons may have enough thermal energy to overcome the gap between the valence and conduction band, consequently these electrons will be detected the same way as electrons which have been excited by photons. They give rise to the so called dark current which is extremely dependent on temperature [45]

$$I_{dark}(T) \propto T^{\frac{3}{2}} \exp(-E_g/2kT) \tag{3.16}$$

The dark current is in good approximation independent on exposure time, therefore the signal due to this current increases linearly with it. Readout noise is always present and not dependent on the signal or the exposure time.

The light intensity falling onto a pixel of the CCD chip is transferred by the cameras electronic into *Counts*, sometimes also called *Analog Digital Units* (ADU). A CCD works in principle as follows. Photons impinging on the chip of the camera excite electrons from the valence band to the conduction band. These electrons gather on the corresponding pixel until the exposure time is finished. These electrons are then transferred to the readout amplifier and the number of electrons will be converted into counts. In this step also the readout noise is added to the signal. The conversion factor from electrons into counts is called gain and is an important number for the estimation of the quantum efficiency of the camera, see section 3.6.2. For our camera the gain can be adjusted in the software in the range of 0.7 to 30, but care has to be taken, since this is not the real conversion factor. For a measurement the gain factor in the camera software was set to one. Information about the gain factor can be acquired by recording the cameras noise in dependence of the signal. Let us first consider the noise of the number of electrons. Since the different noise sources are independent of each other their squares have to be added in order to get the total noise σ_{total}[46].

$$\sigma_{total}^2 = \sigma_S^2 + \sigma_0^2 \tag{3.17}$$

σ_S is that part of the noise which is directly connected to the photon noise, readout noise and thermal noise have been absorbed in σ_0, since they are not dependent on the signal. Since the photon noise follows a poisonian statistic σ_S^2 is equal to the mean number of electrons N_{e^-}.

This can also be expressed in terms of counts by using the gain factor

$$(g\sigma_{counts_{tot}})^2 = gN_c + \sigma_0^2 \tag{3.18}$$

N_c equals the number of counts. It follows $\sigma_{counts_{tot}}^2 = \frac{1}{g}N_c + \frac{1}{g}\sigma_0^2$. Consequently, the gain is given by the inverse slope when plotting the variance of the counts versus the mean value.

Such an analysis was performed with our camera by shining a laser beam continuously on the chip of the camera. The exposure time was chosen to be 20 ms and 100 pictures have been taken under these conditions. The laser intensity was adjusted that the maximum count number was high but not saturating the camera. Afterwards the laser was switched off and 100 pictures were made, from which an average background was deduced. For the evaluation two adjacent pictures were taken and the mean and variance were calculated

$$\bar{x} = \frac{x_1 + x_2}{2} \qquad \sigma^2 = \frac{(x_1 - x_2)^2}{2} \tag{3.19}$$

for each pixel. This was repeated for all pictures. Figure 3.17 shows a plot of the variance versus the mean count number. The data fits well to a linear function as predicted by theory.

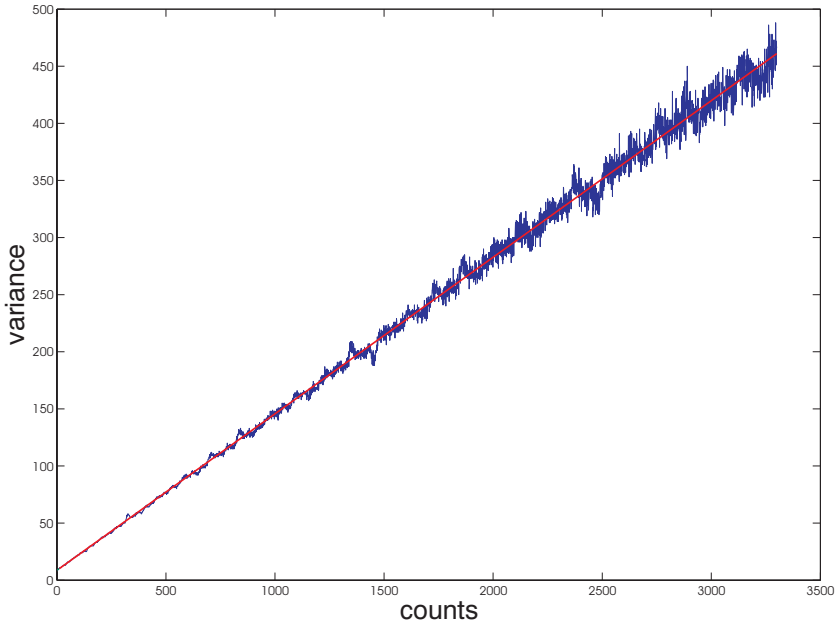

Figure 3.17: Variance versus mean count number. The data fits well to the function $f(x) = ax + b$ with $a = 0.1371 \pm 0.0003$ and $b = 8.621 \pm 0.516$. This results in a gain of $g = 1/a = 7.294 \pm 0.016$.

The gain is, as mentioned above, given by the inverse slope of the linear function. The fit results in a gain of

$$g = \frac{1}{a} = (7.294 \pm 0.016)\,\frac{\text{electrons}}{\text{count}}. \tag{3.20}$$

The fact that the data is well described by a linear function tells us even more. It means that the camera is limited by the photon noise and not by internal noise sources. Therefore this camera can be called shotnoise limited.

3.6.2 Quantum efficiency

Another number characterizing a CCD camera is the quantum efficiency. It describes the probability that an incident photon excites an electron from the valence into the conduction band. This feature is of utmost importance in the field of cold atoms, especially for single atom detection, since low photon numbers must be detected. The higher the quantum efficiency the better the camera is suited for this application. This value was measured for our camera by illuminating the chip with light pulses of well defined duration and power. A sketch of the setup for this measurement can be found in Figure 3.18. Central element of this setup is a computer, which is connected to a

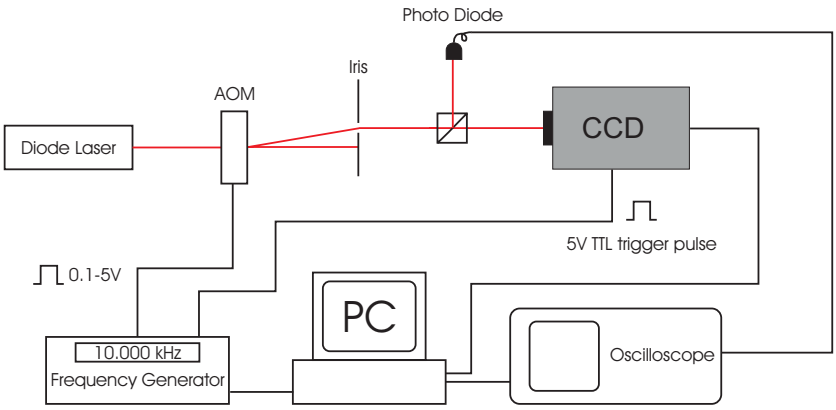

Figure 3.18: Setup for measuring the quantum efficiency of the CCD camera

frequency generator via a GPIB (General Purpose Interface Bus) interface. When the frequency generator gets the start signal from the computer, it sends a TTL triggering signal to the camera. The duration of the pulse determines the exposure time. For this measurement the pulse length was 100 μs. At the same time a second pulse with variable voltage is being sent to the AOM driver. The length of this pulse was 50 μs and its phase was adjusted in a way that the signal lay within the pulse for the camera. The zeroth diffraction order of the AOM was shielded by an iris so that only the first order impinged onto the camera. The intensity of the light pulse is dependent on the voltage of the signal going to the AOM driver.
It is necessary to know how many photons reached the CCD during such a pulse. For this reason a part of the light propagating into the direction of the camera was coupled out with a non polarizing beamsplitter. With the help of a powermeter it is then possible to convert the voltage on the photodiode into power. A calibration of the relation between power in the beam and voltage on the photo diode was done before and after the experiment by changing the voltage going to the AOM driver and measuring the power impinging on the camera. This was done in continuous operation of the AOM, but this is justified as the splitting of the beam at the beamsplitter is the same whether the AOM is pulsed or not. Within the errors the two calibrations yielded the same results. Figure 3.19 a) shows a calibration curve.

The oscilloscope was also connected to the computer via GPIB and the voltage on the photodiode was saved for each pulse. The voltage on the AOM driver was changed between 0.1 V and 5 V in steps of 0.1 V, repeating the ramp for five times.
The evaluation was done in the following way. For each image the total number of counts was calculated by summing over the picture. A mean background picture as mentioned in the previous subsection was subtracted beforehand. With the help of the calibration curve it is possible to convert the voltage on the photodiode into power on the camera. The number of photons is then given by

$$N_{phot} = \frac{P\Delta t\lambda}{hc} \tag{3.21}$$

where Δt is the length of the light pulse, in our case this was 50 μs. The wavelength λ of the laser was 780 nm. h is Planck's constant and c the speed of the light. The number of counts and the number of photons is connected via

$$N_{counts} = \frac{\eta}{g} N_{phot} \quad \Rightarrow \quad \eta = g\frac{N_{counts}}{N_{phot}} \tag{3.22}$$

where g is the gain determined in the last subsection.

Figure 3.19 b) depicts the number of counts N_{counts} plotted versus the number of photons N_{phot}.

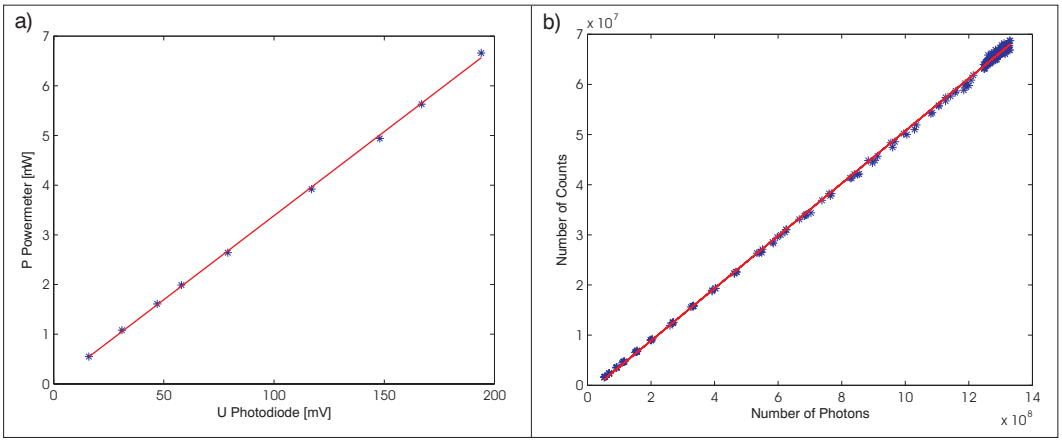

Figure 3.19: a) Typical calibration curve voltage on photodiode - power incident on the camera b) Number of counts versus number of photons. The data fits well to a linear function with a slope of 0.0523 ± 0.0017.

The data points can be very well described by a linear fit with a slope of

$$(0.0523 \pm 0.0017)\,\frac{\text{counts}}{\text{photons}}. \tag{3.23}$$

The error takes also the imprecision of the powermeter into account, which is specified as ±3%. The accumulation of points at higher photon numbers is due to a saturation effect of the AOM. Above a certain voltage the diffraction efficiency does not increase anymore but stays constant. The negative offset in Figure 3.19 b) is reasoned by rounding errors while computing the averaged background picture, however this offset is not important the solely interesting figure is the slope. Using (3.22) and the result for the gain in the last subsection yields a quantum efficiency of

$$\eta = (38.15 \pm 1.25)\,\% \tag{3.24}$$

4 Generation of Dark Soliton Fans - A preliminary Experiment

In this part an experiment observing dark soliton fans in a trapped Bose-Einstein Condensate is presented. The BEC is prepared in a double-well potential and after switching off the barrier the two modes localized in the left and right well expand and interfere. Due to the repulsive interaction between the atoms the minima in the interference pattern are emerge into to dark solitons. First a short introduction into the theoretical description of BEC dynamics and the phenomenon of dark solitons will be given. Afterwards the results of the experiment on this topic are presented and compared to numerical simulations.

4.1 Gross-Pitaevskii Equation and Dark Solitons

The phenomenon of Bose-Einstein Condensation corresponds to the macroscopic occupation of the ground state below a certain critical temperature T_c. For a detailed description of this topic please refer to textbooks as [18, 15, 35] or to the original publications of Bose [6] and Einstein [5]. Here I will concentrate on the dynamics of the condensed state which is described by the *Gross-Pitaevskii Equation* (GPE) that was first developed by Gross [47, 48] and Pitaevskii [49]. An accurate formulation of the temporal evolution of a BEC must take into account the interaction between single atoms. This is fulfilled in the GPE by a mean-field-approach comparable to the Hartree-Fock calculation in the theory of many-electron atoms. The time dependent GPE is given by

$$i\hbar\frac{\partial}{\partial t}\Psi(\mathbf{r},t) = \left(-\frac{\hbar^2\nabla^2}{2m} + V_{ext}(\mathbf{r},t) + g|\Psi(\mathbf{r},t)|^2\right)\Psi(\mathbf{r},t) \tag{4.1}$$

where $g = 4\pi\hbar^2 a/m$ is the coupling constant determined by the s-wave scattering length a whose sign determines whether the interaction is attractive (-) or repulsive (+). This is a Schrödinger equation of a particle in a potential being the sum of the external potential V_{ext} and an additional contribution due to interaction which is proportional to the particle density $n(\mathbf{r},t) = |\Psi(\mathbf{r},t)|^2$. This nonlinear term gives rise to many new effects, (dark) solitons being one of the paradigm examples.

In the stationary case, one can separate the spatial and the time dependence by the following ansatz:

$$\Psi(\mathbf{r},t) = \Psi(\mathbf{r})e^{-i\mu t/\hbar}. \tag{4.2}$$

Inserting this into (4.1) one gets

$$\mu\Psi(\mathbf{r},t) = \left(-\frac{\hbar^2\nabla^2}{2m} + V_{ext}(\mathbf{r},t) + g|\Psi(\mathbf{r},t)|^2\right)\Psi(\mathbf{r},t). \tag{4.3}$$

It is important to note that the phase evolution of a stationary state is not governed by the energy, but by the chemical potential.

One-dimensional Gross-Pitaevskii Equation

To understand the basic principles of dark soliton theory it is sufficient to consider the one dimensional case. Therefore I will first discuss the reduction of the GPE from three to one dimension. One assumes a potential which is harmonic in the transverse and of arbitrary shape in x-direction. Hence, the potential has the following form

$$V_{ext}(\mathbf{r},t) = V_{ext}(x,t) + \frac{1}{2}m\omega_\perp^2(y^2+z^2). \tag{4.4}$$

The wave function is assumed to be of gaussian shape in the transverse direction. Hence, one makes the following ansatz

$$\Psi(\mathbf{r},t) = \frac{1}{\sqrt{\pi\sigma_\perp^2}}\Psi(x,t)\exp\left(-\frac{y^2+z^2}{2\sigma_\perp^2}\right). \tag{4.5}$$

The transverse width $\sigma_\perp$ is assumed to be constant and equal to the groundstate width of a harmonic oscillator

$$\sigma_\perp = \sqrt{\frac{\hbar}{m\omega_\perp}}. \tag{4.6}$$

.

Inserting this ansatz into the 3D-GPE (4.1) and integrating over the y and z-direction yields

$$i\hbar\frac{\partial}{\partial t}\Psi(x,t) = \left(-\frac{\hbar^2}{2m}\frac{\partial^2}{\partial x^2} + V_{ext}(x,t) + g_{1d}|\Psi(x,t)|^2\right)\Psi(x,t) \tag{4.7}$$

where g_{1d} is an effective one-dimensional interaction constant, given by $g_{1d} = 2a\hbar\omega_\perp$.

The interaction couples the dynamics of the condensate in all three spatial directions, leading to a restriction on the validity of equation (4.7). It is only applicable when the

interaction energy is small compared to the energy of the transverse energy of the ground state. In terms of the s-wave scattering this can be expressed as $a|\Psi(x,t)|^2 \ll 1$.

Dark Solitons

In the case of a uniform Bose gas the *One-dimensional Gross-Pitaevskii Equation* (4.7) has analytical solutions in form of solitary waves. The character of solitons is that their shape does not change in time. [1] There are two types of solitons, namely bright and dark solitons. Bright solitons correspond to a wave packet not dispersing while propagating. From a first point of view they are expected for particles with attractive interaction which can compensate the effects of dispersion. They can also be generated in the presence of repulsive interaction as shown in [50]. On the other hand, dark solitons correspond to a suppression of the atom density with respect to its bulk value n_0. Here the repulsive interaction trying to decrease the minimum is compensated for by the phase gradient enhancing the minimum. The solution of (4.7) in a uniform Bose Gas involving a dark soliton has the form [51]

$$\Psi(x-vt) = \sqrt{n_0}\left[i\frac{v}{c} - \sqrt{1-\frac{v^2}{c^2}}\tanh\left(\frac{x-vt}{\sqrt{2}\xi}\sqrt{1-\frac{v^2}{c^2}}\right)\right] \tag{4.8}$$

where $c = \sqrt{4\pi a n_0}\hbar/m$ is the velocity of sound and $\xi = (4\pi a n_o)^{-1/2}$ the healing length. Figure 4.1 shows the density profile for two different velocities. The density profile $n = |\Psi|^2$ has a minimum in the middle $n(0) = n_0(v^2/c^2)$ and the phase of the wave function undergoes a finite change $\Delta\Phi$ as x varies from $-\infty$ to $+\infty$ of

$$\Delta\Phi = 2\arccos\left(\frac{v}{c}\right) \tag{4.9}$$

For a black (stationary) soliton the wave function is real having a zero crossing at the position of the soliton, accompanied by a sharp phase jump of π.

4.2 A preliminary Experiment

We performed a preliminary experiment concerning the generation of dark soliton fans [22]. Since our experimental setup has been described in previous works [29, 30], I will only consider these parts which are important for this measurement. The first step is the preparation of a Bose-Einstein Condensate consisting of about 2000 atoms in an optical dipole trap, established by two crossing laser beams provided by a Nd-Yag Laser running on a wavelength of 1064 nm. The trapping frequencies are $\omega_x = 2\pi \times 35(1)$

[1] Actually, the strict definition of solitons concerns collisions between them. Only when the number of degrees of freedom is equal to the number of conserved quantities the structures are the same before and after the collision and one speaks about solitons.

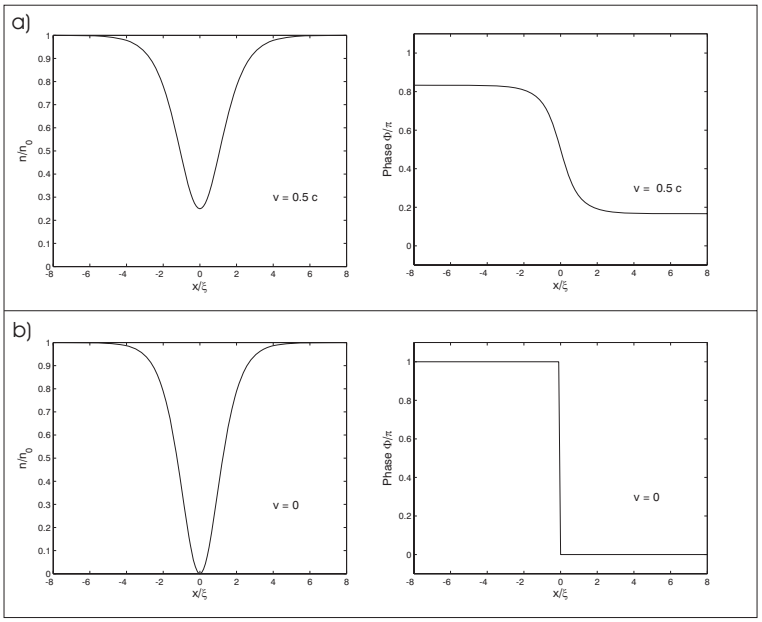

Figure 4.1: Density and phase profile for dark solitons with two different velocities a) $v = 0.5c$ *grey soliton* b) $v = 0$ *black soliton*

Hz, $\omega_y = 2\pi \times 77(1)$ Hz and $\omega_z = 2\pi \times 77(1)$ Hz. Then a 1d-optical lattice in x-direction is ramped up which is produced by interference of two additional laser beams crossing under an angle of approximately ten degrees. The wavelength of these beams is 829.739 nm resulting in a lattice spacing of 4.8 μm. By addition of the parabolic potential in x-direction and the optical lattice we get an effective double well potential with a well distance of 4.46 μm, (see Figure 4.2). The mathematical expression for the

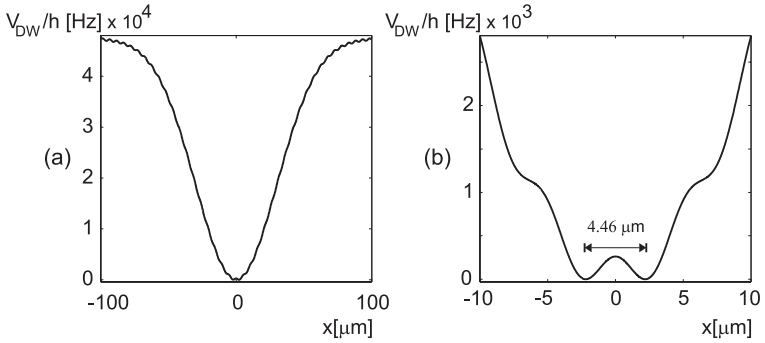

Figure 4.2: a) dipole potential resulting from the addition of the parabolic potential and the 1d-lattice b) magnification of the central region in a) revealing the effective double-well

resulting potential in x-direction is given by

$$V(x) = \frac{1}{2} m\omega_x^2 x^2 + \frac{V_0}{2} \left(1 + \cos(2\pi x/q)\right). \tag{4.10}$$

In the experiment the standing light wave was ramped up to a value of $V_0 = 610$ Hz leading to the occupation of only two wells. When the double-well is prepared the standing light wave is switched off as fast as possible and at the same time the confinement in x-direction is lowered to $2\pi \times 12(1)$ Hz within a ramp of 14 ms. This is done in order to prevent quadrupole oscillations of the cloud. The two matterwave packets collide and interfere. The minima of the interference pattern are then formed into dark solitons due to the interaction between the particles and start to oscillate in the trapped Bose-Einstein Condensate.

Figure 4.3 shows the result of a full 3d simulation of the Gross-Pitaeevski Equation for the experimental protocol given above. The simulation was done by applying a split-step Fourier method. Part a) shows the spatialtemporal evolution of the atom density.

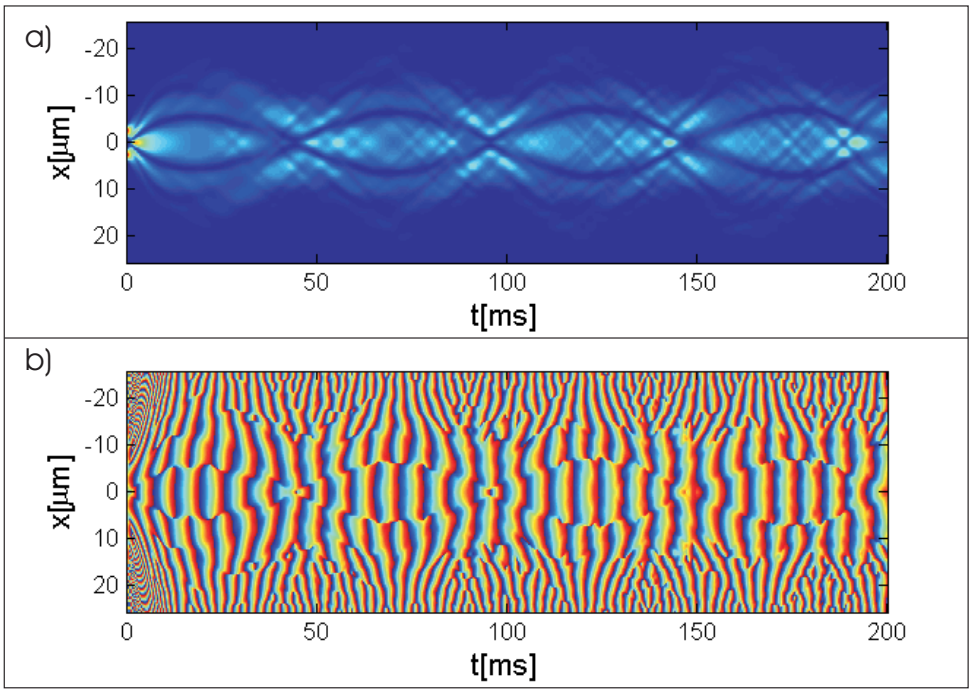

Figure 4.3: a) Spatialtemporal plot of the atomic density obtained from a numerical solution of the three-dimensional Gross-Pitaevskii Equation b) Phase of the wavefunction, the phase jump confirms the generation of dark solitons

Obviously two density minima oscillate in the trap. In b) the phase of the wave function is plotted, revealing a phase jump at the position of the density minima, what is an indication for the generation of dark solitons.

In Figure 4.4 our experimental results are compared with the simulation for three different evolution times. The first row shows the experimentally achieved density profile. This profile is acquired by summing over three central lines of the 2d picture of the atom distribution. The second row shows the simulated density profile, while the third one depicts the phase of the wavefunction also resulting from the simulation. For T=72 ms the

phase jump of nearly π at the position of the soliton is obvious. The accordance between simulation and experiment is not perfect, but when taking our resolution of 3.5(2) μm into account and considering the fact that our imaging beam is not perpendicular to the x-direction but tilted by 12.3°, this is at least an indication for the creation of dark solitons oscillating in the trap.

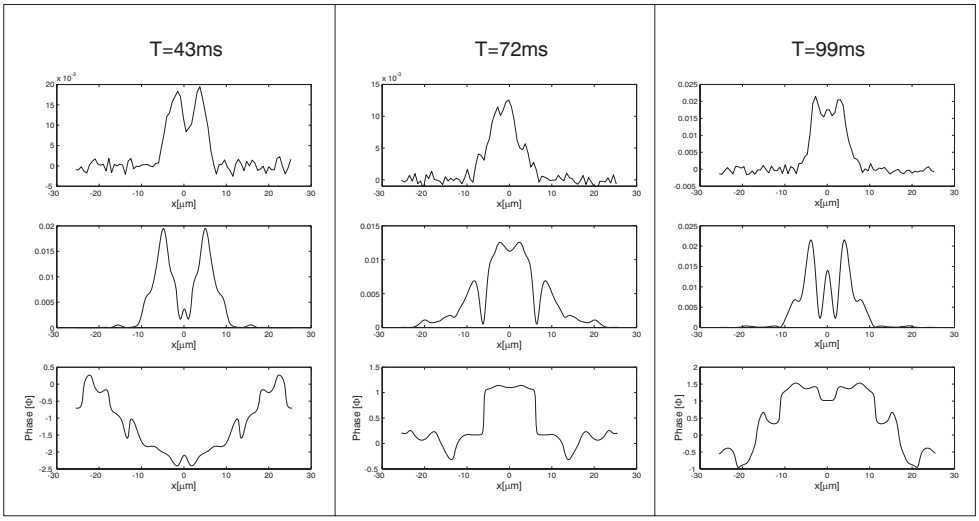

Figure 4.4: First row: measured density profile, second row: density distribution according to the simulation, third row: simulated phase of the wavefunction

Figure 4.5 shows the distance of the experimentally observed density minima in dependence of time. A sinusoidal fit yields a period of 109±4 ms, what is a factor of 1.31±0.05 bigger than the period of dipolar motion, which is 83.3 ms. The result of the simulation shown before, yields a period of 104±2 ms. Within the errors this is in agreement with the experimentally acquired value.

The deviation of the oscillation time of the solitons from the trapping frequency is theoretically expected. As shown in [52] the oscillation period of a single dark soliton in a trapped 1d-Bose-Einstein Condensate should be a factor of $\sqrt{2}$ bigger than the dipolar motion of the condensates. In our experiment we have at least two solitons in the trap oscillating against each other so that also a possible interaction of the solitons must be considered [53]. Two dark solitons interact through a short-range repulsive, but finite potential depending on velocity. Therefore two solitons can, depending on their energy, perform crossings or avoided crossings which leads to a deviation from the factor of $\sqrt{2}$ to lower values [54]. It must also be stated that the geometry of our trap is not 1d and that therefore different results are expected.

The reason why the results presented here can only be called preliminary is that the spatial extend of the solitons is on the order of the healing length requiring an imaging system with a high spatial resolution. At the time when this measurement was performed our resolution was 3.2(2) μm which is on the edge of the requirements. Another problem

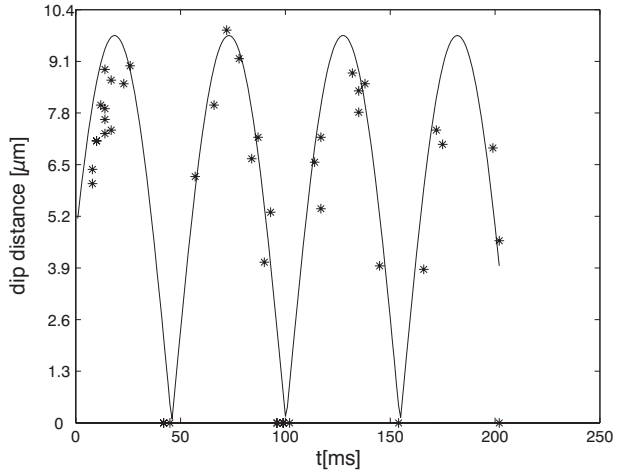

Figure 4.5: Distance of the density minima in dependence of time. The points denote the experimental results, the curve is a fit of the form $f(x) = a|\sin(2\pi/T + c)| + d$, yielding an oscillation time of 109 ± 4 ms

inherent to this method of generating dark solitons is the interference itself more precisely its dependence on the relative phase of the two wave packets. As shown in [55] and experimentally confirmed in [11, 12, 13] the relative phase underlies fluctuations due to finite temperature. These fluctuations increase with temperature and decrease with tunneling coupling. As the relative position of the interference fringes with respect to the envelope depend on the relative phase accurate parameters for the barrierheight must be found in order to get symmetric interference patterns not too much varying from shot to shot. In Figure 4.4 the atom density at T=72 ms is not symmetric due to this effect. A detailed discussion of thermal fluctuations in a double-well potential can be found in [12].

5 Conclusion and Outlook

The main aim of this thesis was the development and test of an objective for high resolution imaging of Bose-Einstein Condensates (BEC). As described in the theory part, a characterizing property of an imaging system is its Point Spread Function (PSF). This function describes what the image of a single point (δ-excitation) in the object plane looks like. For a diffraction limited system this function is given by the Airy diffraction pattern of the lens aperture. The resolution is commonly defined by the minimal distance which two points in the object plane may have, so that they are still distinguishable in the image. According to the Rayleigh criterion this is the distance between the central maximum and the first minimum of the Airy diffraction pattern. This distance increases proportional to the wavelength of the light used for illumination of the sample and decreases proportional to the inverse of the numerical aperture *NA* of the imaging optics, which is basically determined by the focal length and the front diameter of the lens system. The numerical aperture of our new objective, which was designed in collaboration with *Carl Zeiss Laser Systems* is specified as 0.45, accounting for a theoretical resolution of 1.1 μm for the used wavelength of 780 nm.
Experimentally, the resolution was estimated with a simple test setup. Since the objective was actually designed for focusing a collimated beam, the sample is placed in the focal plane of the objective corresponding to a transformation of the object to infinity. The backtransformation is done with an additional achromatic lens that projects the image on a CCD camera. Since the experiments concerning Bose-Einstein Condensation are performed in an ultra high vacuum glass cell, a glass plate made of the same material as the cell and with the same thickness was placed between the sample and the objective. The magnification of the system is determined by the ratio of the focal lengths of the objective and the additional achromat. Using a standard objective micrometer scale with a line spacing of 10 μm, a value of 11.18$\pm$0.03 was acquired, which is in very good agreement with the theoretical value.
For an evaluation of the resolving power, a gold grating consisting of holes with a diameter of 650 nm separated by 20 μm was used. This data was acquired by examination of the grating with a scanning electron microscope. The resolution was then estimated by doing a 2-d best fit analysis, comparing real images of one hole with the result of a numerical simulation. In this simulation the hole was approximated by a circle with the same diameter as the hole. The imaging process was simulated by convolving this circle with point spread functions of Airy form, varying the resolution, and computing the root mean square deviation from the real picture. This deviation turned out to be minimal for a resolution of 1.1(1) μm, which means the realization of a diffraction limited imaging system with high resolution.

This result was confirmed in a more direct way by making use of the so-called Talbot Effect. This effect corresponds to the production of self-images of a grating by diffraction. At certain distances behind the grating, which are an integer multiple of the so-called *Talbot length* the intensity distribution is a reproduction of the grating. At fractional multiples of this distance also grating structures are produced but with a grating constant being only a fraction of the original one. This was utilized to generate a grating structure of 1 μm. An image of this pattern revealed clear modulations on the scale of 1 μm, confirming the result of the best fit analysis.
Additional measurements concerning astigmatism, field of view and a possible tilt between the objective and the glass cell have been performed. The amount of astigmatism was estimated by moving the objective with the help of a motorized translation stage with respect to the grating and fitting gaussian envelopes in x- and y-direction to the recorded intensity distribution. When no astigmatism is present the focus is well defined and the waists for both directions are minimal at the same point. In the case of astigmatic aberration the position of minimal waist is different for both directions. This effect was also observed with our test setup, 20 μm away from the optical axis a splitting of the focus position was apparent. This result could not be improved with the simple test setup. Most likely this aberration is due to an off-centering or tilt of the additional achromat with respect to the objective. For the final setup both the objective and the achromat should be mounted in the same part, ideally machined in one clamping in order to reach a nice centering.
The field of view (FOV) is defined as the region in the object plane, in which the imaging system produces a sharp picture. The grating is an ideal test object for such an evaluation, as it provides a large area with equally spaced small holes. To get an idea about the FOV gaussian envelopes were fitted to a picture of the whole grating. Due to the astigmatism mentioned above only a rough estimation was possible based on the fitted waists in x-direction, yielding field of view with a diameter of about 400 μm.
The influence of a tilt of the objective with respect to the glass cell was studied by tilting the glass plate in the test setup. Already a tilt of 0.2 degrees lead to a tail in the image of the holes on the grating. Hence, in the final setup it must be possible to align the angle between the objective and the glass cell.
A feasible solution for the final installation of the objective in the experimental setup has been given. All commercially available parts for the setup have been ordered, but have not yet arrived. The other parts will be machined in the workshop of the institute, as soon as possible.

The second part of this thesis deals with a preliminary experiment for the generation of dark soliton fans. The first step in the experimental procedure is the preparation of a Bose-Einstein Condensate in a double-well potential, leading to two localized modes in the two wells. After switching off the barrier, the two matterwave packets collide and form interference fringes whose minima are transformed to dark solitons due to the interaction between the atoms. These solitons then start to oscillate in the trap. A numerical simulation of the experiment has been done by solving the three dimensional *Gross-Pitaevskii Equation* with a split-step Fourier method. This simulation revealed at

least two oscillating density minima, accompanied by a phase jump, what is an indication for the generation of dark solitons. The observation of these density minima in the real experiment with the current setup is difficult as our optical resolution is at the moment only 3.5(2) μm, but oscillating density minima have been observed, although the structures are smeared out due to the imaging. An analysis of the dip distance in dependence of time, yielded a deviation from the trapping frequency by a factor of 1.31(5). Theoretical considerations [52] lead to a factor of $\sqrt{2}$, but this is only valid in a 1-d situation and for a single soliton in the trap. This is not true for our experiment. Our trapping geometry does not allow a one dimensional description and the interaction between the two generated solitons can lead to a deviation from this factor of $\sqrt{2}$. These are only first results and the experiment should be repeated when the new imaging system is installed. The higher resolution will make quantitative measurements possible.

Outlook

The high resolution of the imaging system developed during this thesis enables the observation of structures in a BEC which occur on the order of the healing length, which is the typical length scale on which density variations in the BEC occur. Among these structures are, as already mentioned, dark solitons or vortices. The new lens system enables to observe the oscillation of the solitons in the trap in more detail. A more precise measurement of the oscillation period and the amplitude in dependence of time will be possible. The amplitude should increase as the solitons lose energy by the emission of soundwaves and become shallower. Another possible application is the detection of single atoms. Hence, the observation of density fluctuations and the measurement of the density correlation function with high precision will be feasible. Such a measurement has already been performed [40], but with poorer optical resolution. Also Laughlin states of atoms in optical lattices [56] could be observable. These states are also known from the fractional quantum Hall effect in solid state physics.

The lens system can also be used for the generation of arbitrary potentials that are superimposed to the current potential. Due to the small focus each well in the double-well potential can be addressed separately. Thus, it is possible to imprint arbitrary phases onto one mode of the BEC. This enables to observe so-called π-oscillations [57], which have not been observed so far. Also ring dark solitons [58] can be created which require a circular phase imprinting pattern. Using this phase imprinting device for creating a thin, quickly removable barrier in an otherwise harmonic confinement, represents another method to study the collision of two Bose-Einstein Condensates and the observation of dark soliton fans that is less sensitive on phase fluctuations.

A Technical Drawings

In this Appendix the technical drawings of all objective components are presented.

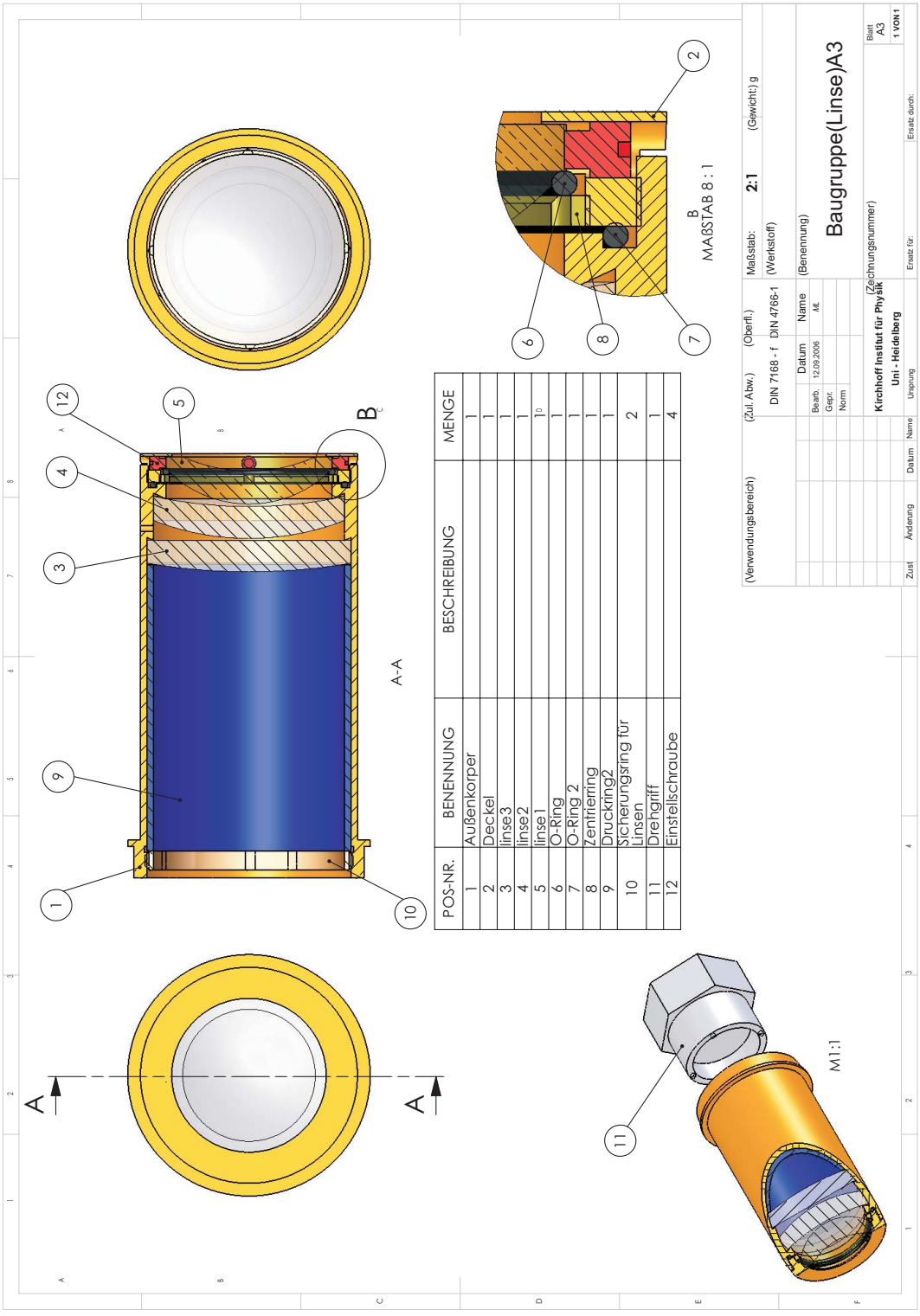

Figure A.1: All components in their objective configuration

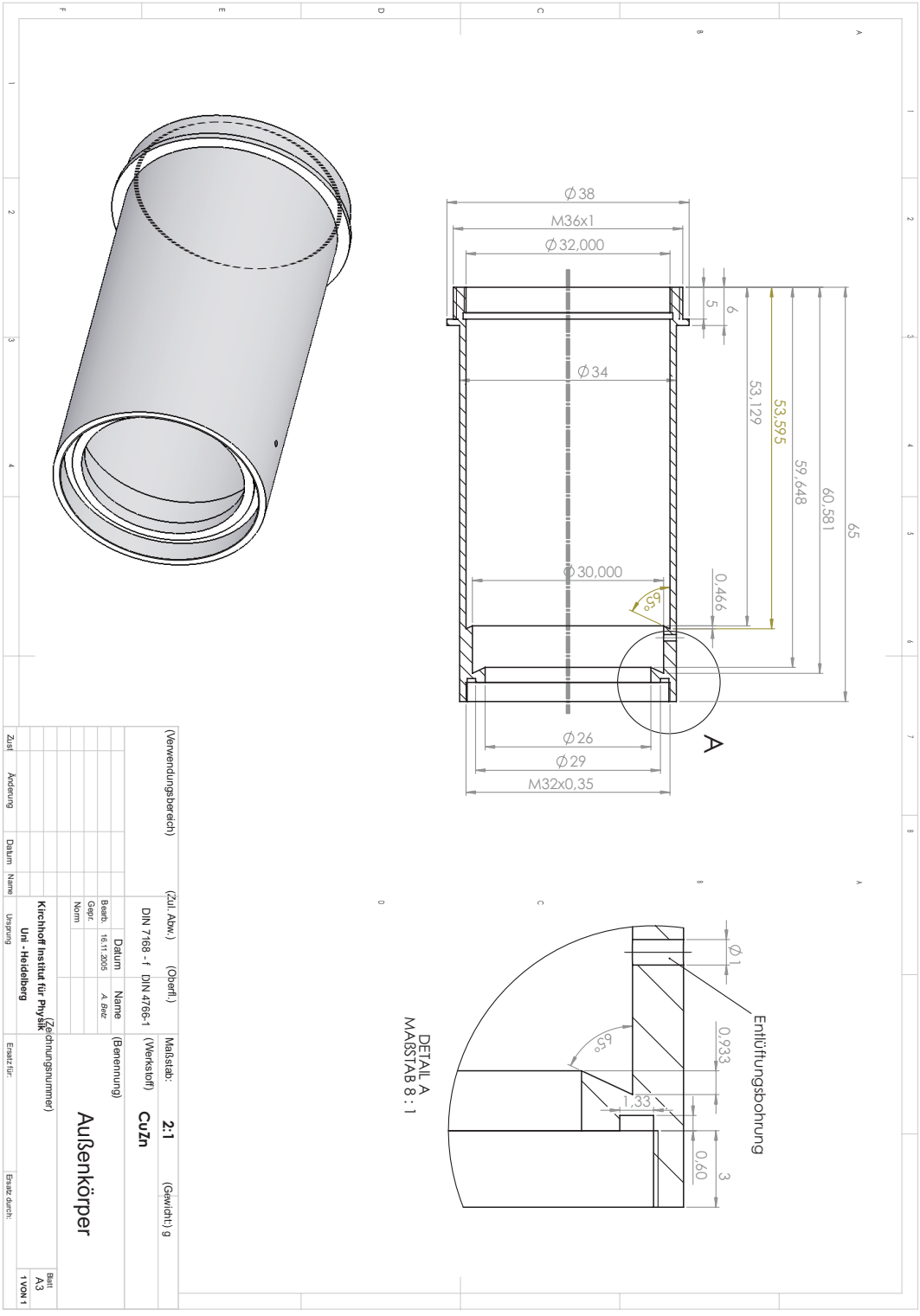

Figure A.2: Technical drawing of the first part of the lens mount accommodating lenses two and three

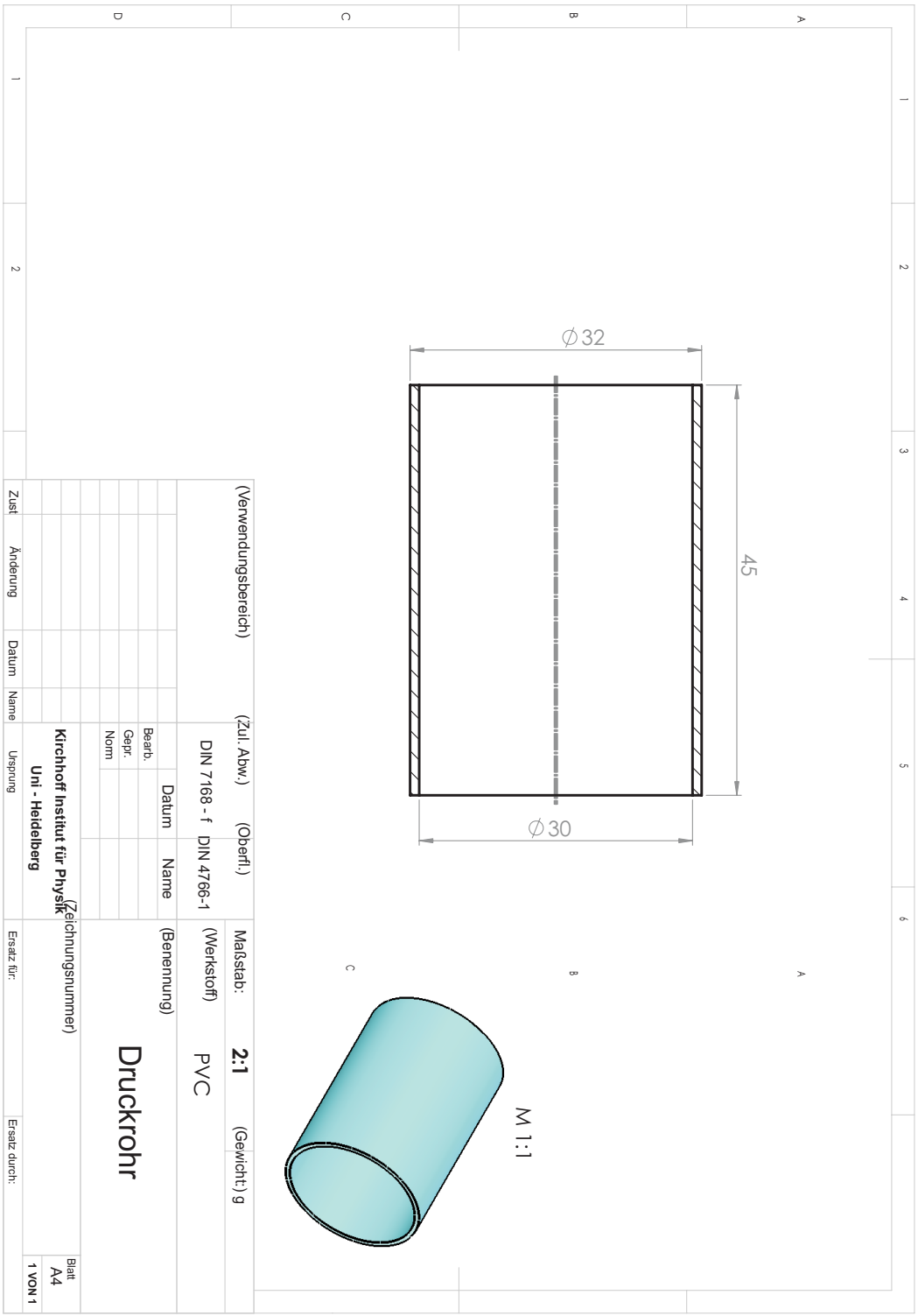

Figure A.3: Plastic tube for clamping lens three

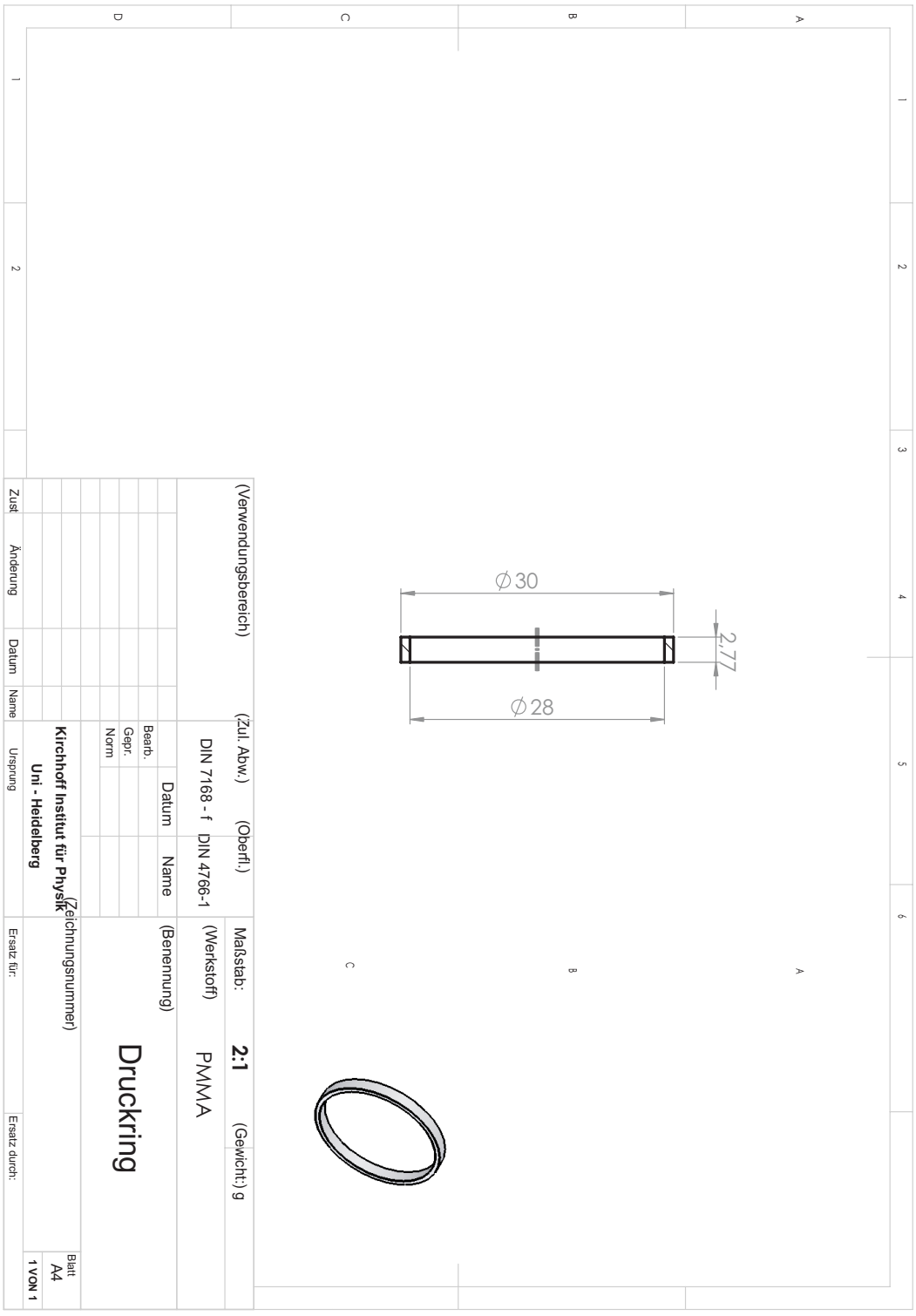

Figure A.4: Clamping ring for tube

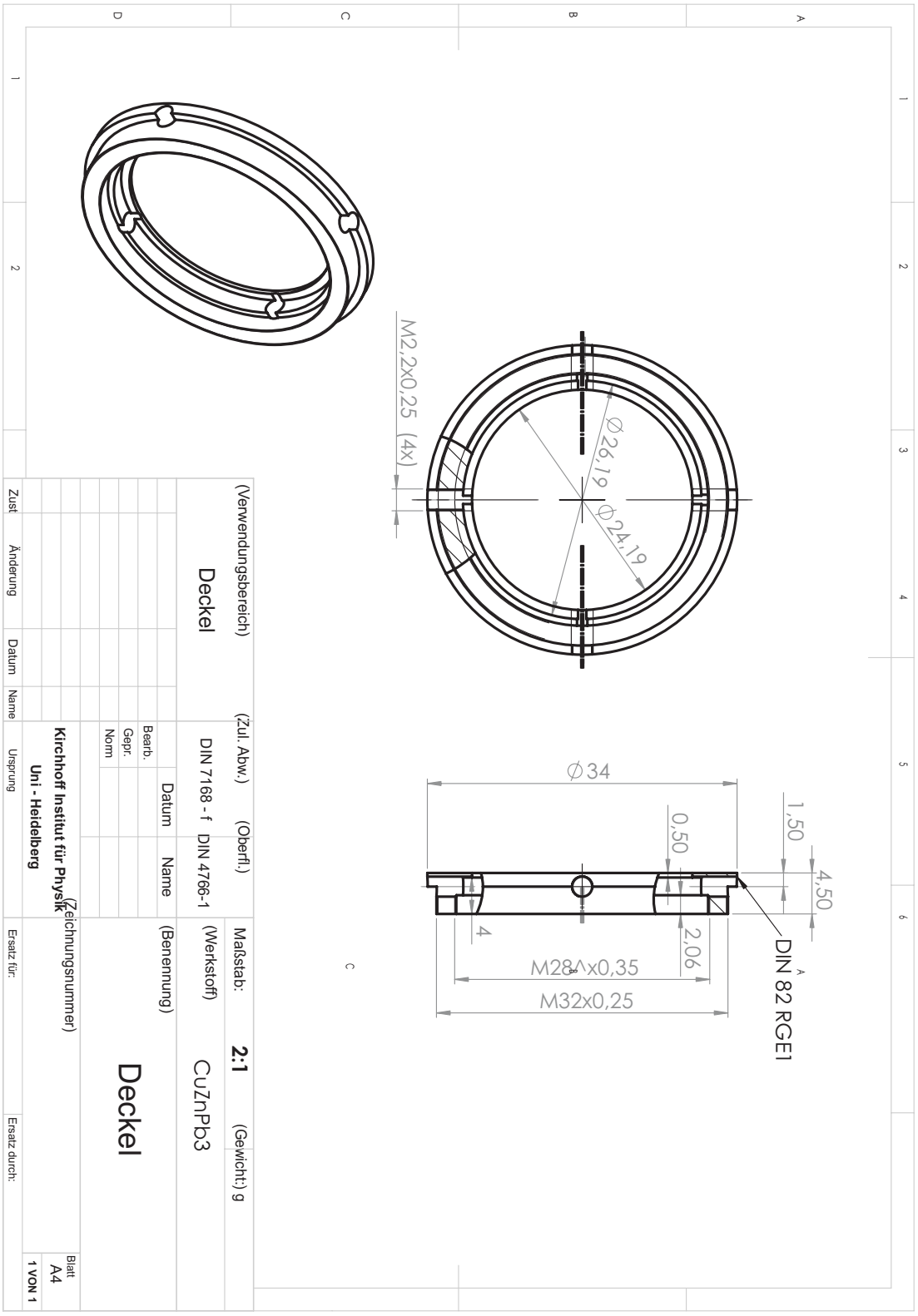

Figure A.5: Component for mounting lens one

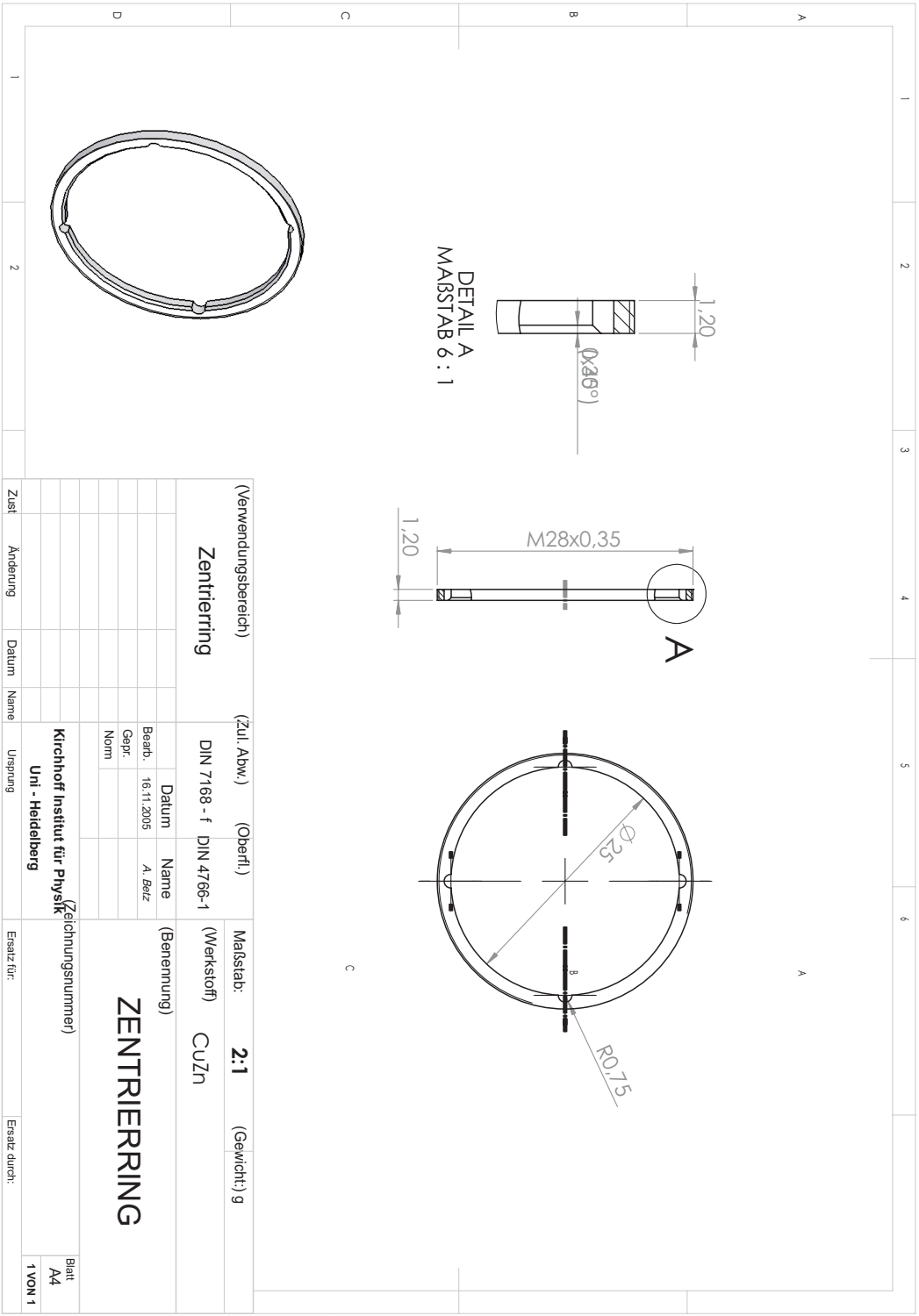

Figure A.6: Clamping ring for lens1

Bibliography

[1] G. Davisson and L.H. Germer. Diffraction of Electrons by a Crystal of Nickel. *Physical Review*, **30**:705, 1927.

[2] L. DeBroglie. A Tentative Theory of Light Quanta. *Phil. Mag.*, **47**:446, 1924.

[3] B.D. Josephson. Posssible New Effects in Superconductive Tunneling. *Physics Letters*, **1**:251–253, 1962.

[4] P.L. Anderson and J.W. Rowell. Probable Observation of the Josephson Superconducting Tunnel Effect. *Physical Review Letters*, **10**:230, 1963.

[5] Albert Einstein. Quantentheorie des einatomigen idealen Gases. Zweite Abhandlung. *Sitzungsberichte der Preussischen Akademie der Wissenschaften*, **1**:3, 1925.

[6] N. S. Bose. Plancks Gesetz und Lichtquantenhypothese. *Z. Phys.*, **26**:178, 1924.

[7] K. Davis, M.-O. Mewes, M. Andrews, N. van Druten, D. Durfee, D.M. Kurn, and W. Ketterle. Bose-Einstein Condensation in a Gas of Sodium Atoms. *Physical Review Letters*, **75**:3969, 1995.

[8] M. Anderson, J. Encher, M. Matthews, C. Wiemann, and E. Cornell. Observation of Bose-Einstein Condensation in a Dilute Atomic Vapor. *Science*, **269**:198, 1995.

[9] C.C. Bradley, C.A. Sackett, J.J. Tollet, and R.G. Hulet. Evidence of Bose-Einstein Condensation in an Atomic Gas with Attractive Interactions. *Physical Review Letters*, **75**:1687, 1995.

[10] M.R. Andrews, C.G. Townsend, H.-J. Miesner, D.S. Durfee, D.M. Kurn, and W. Ketterle. Observation of Interference Between Two Bose Condensates. *Science*, **275**:637, 1997.

[11] R. Gati, B. Hemmerling, J. Fölling, M. Albiez, and M.K. Oberthaler. Noise Thermometry with Two Weakly Coupled Bose-Einstein Condensates. *Physical Review Letters*, **96**:130404, 1996.

[12] B. Hemmerling. Thermally Induced Fluctuations in a Bosonic Josephson Junction. Diploma thesis, University of Heidelberg, 2006.

[13] R. Gati, J. Esteve, B. Hemmerling, T.B. Ottenstein, J. Appmeier, A. Weller, and M.K. Oberthaler. A primary noise thermometer for ultracold Bose gases. *New Journal of Physics*, **8**(9):189, 2006.

[14] M. Albiez, R. Gati, J. Fölling, S. Hunsmann, M. Cristiani, and M.K. Oberthaler. Direct Observation of Tunneling and Nonlinear Self-Trapping in a Single Bosonic Josephson Junction. *Physical Review Letters*, **95**:0104020, 2005.

[15] L. Pitaevskii and S. Stringari. Bose-Einstein Condensation. Oxford University Press, Oxford, New York, 2003.

[16] W. Alt. An objective lens for efficient fluorescent detection of single atoms. *Optik*, **113**(3):142–144, 2002.

[17] P. Baranowski, J. Zacks, G. Hechenblaikner, and C.J. Foot. Testing and design of a lens system for atom trapping and fluorescence detection, arXiv:physics/0412126 v1. 2004.

[18] F. Schwabl. Statistische Mechanik. Springer-Verlag, Berlin, Heidelberg, New York, 2000.

[19] J. Denschlag, J.E. Simsarian, D.L. Feder, Charles W. Clark, L.A. Collins, J. Cubizolles, L. Deng, E.W. Hagley, K. Helmerson, W.P. Reinhardt, S.L. Rolston, B.I. Schneider, and W.D. Phillips. Generating Solitons by Phase Engineering of a Bose-Einstein Condensate. *Science*, **287**:97, 2000.

[20] B.P. Anderson, P.C. Haljan, Regal C.A., D.L. Feder, Collins L.A., Clark C.W., and Cornell E.A. Watching Dark Solitons Decay into Vortex Rings in a Bose-Einstein Condensate. *Physical Review Letters*, **86**(14):2926, 2001.

[21] S. Burger, K. Bongs, S. Dettmer, W. Ertmer, and K. Sengstock. Dark Solitons in Bose-Einstein Condensates. *Physical Review Letters*, **83**(25):5198, 1999.

[22] G. Theocharis, P. Schmelcher, M.K. Oberthaler, P.G. Kevrikidis, and D.J. Frantzeskakis. Personal communication.

[23] J. W. Goodman. Introduction to Fourier Optics. McGraw-Hill, Boston, MA, 1998.

[24] M.V. Klein and T.E. Furtak. Optik. Springer-Verlag, Berlin, Heidelberg, 1988.

[25] M.L Boas. Mathematical Methods in the Physical Sciences - 2nd Edition. John Wiley & Sons, Inc., New York, 1983.

[26] E. Hecht. Optics, volume 4. Addison Wesley Longman, Inc., USA, 2002.

[27] W. Demtröder. Experimentalphysik 2 - Elektrizität und Optik, 2. Auflage. Springer Verlag, Berlin, Heidelberg, New York, 2002.

[28] M. Born and E. Wolf. Principles of optics. Campridge University Press, Cambridge, 2002.

[29] B. Eiermann. Kohärente nichtlineare Materiewellendynamik - Helle Atomare Solitonen. PHD thesis, Universität Konstanz, 2004.

[30] M Albiez. Observation of nonlinear tunneling of a Bose-Einstein condensate in a single Josephson junction. PHD thesis, Universität Heidelberg, 2005.

[31] W. Ketterle, D.S. Durfee, and D.M. Stamper-Kurn. Making, Probing and Understanding Bose-Einstein Condensates. In M. Inguscio, S. Stringari, and C. Wieman, editors, *Bose-Einstein Condensation in Atomic Gases*, Amsterdam: IOS Press, 1999. Società Italiana di Fisica.

[32] L.D. Turner, K.F.E.M. Domen, and R.E. Scholten. Diffraction-contrast imaging of cold atoms. *Physical Review A*, **72**:031403, 2005.

[33] H. Talbot. Facts relating to optical science. *Philos.Mag.*, **9**:401, 1836.

[34] J. Fölling. Bose-Einstein Josephson Tunnelling and Generation of Arbitrary Optical Potentials. Diploma thesis, Universität Heidelberg, 2005.

[35] C.J. Pethick and H. Smith. Bose-Einstein Condensation in dilute gases. Cambridge University Press, Cambridge, 2002.

[36] Z. Hadzibabic, P. Krüger, M. Cheneau, B. Battelier, and J. Dalibard. Berezinskii-Kosterlitz-Thouless crossover in a trapped atomic gas. *Nature*, **441**:1118–1121, 2006.

[37] G. Theocharis, P. Schmelcher, M.K. Oberthaler, P.G. Kevrekidis, and D.J. Frantzeskakis. Lagrangian Approach to the Dynamics of Dark Matter-Wave Solitons. *Physical Review A*, **72**:023609, 2005.

[38] W.P. Reinhardt and C.W. Clark. Soliton Dynamics in the Collision of Bose-Einstein Condensates. *J. Phys. B. At. Mol. Opt. Phys.*, **30**:L785, 1997.

[39] T.F. Scott, R.J. Ballagh, and K. Burnett. Formation of Fundamental Structures in Bose-Einstein Condensates. *J. Phys. B. At. Mol. Opt. Phys.*, **31**:L329, 1998.

[40] J. Esteve, J.-B. Trebbia, T. Schumm, A. Aspect, C.I. Westbrook, and I. Bouchoule. Observations of Density Fluctuations in an Elongated Bose Gas: Ideal Gas and Quasicondensate Regimes. *Physical Review Letters*, **96**:130406, 2006.

[41] L. Hackermüller. Realisierung eines Talbot-Lau-Interferometers mit C_{70} Molekülen. Diploma thesis, Universität Wien, 2001.

[42] I.N. Bronstein, K.A. Semendjajew, G. Musiol, and H. Mühlig. Taschenbuch der Mathematik. Verlag Harri Deutsch, Thun und Frankfurt am Main, 2000.

[43] M. Berry and S. Klein. Integer, fractional and fractal Talbot effects. *J. of Mod. Opt.*, **43**:2139, 1996.

[44] B. Rohwedder. Atom Optical Elements Based on Near-field Grating Sequences. *Fortschr. Phys.*, **47**:883–911, 1999.

[45] S. Hippler, W. Brandner, and T. Henning. Skript zum Versuch F36-Teil II 'Wellenfrontanalyse mit einem Shack-Hartmann-Sensor' des Fortgeschrittenen-Praktikums II der Universität Heidelberg für Physiker - *Messung der Charakteristika einer CCD Kamera*. 2006.

[46] M. Newberry. Measuring the Gain of a CCD camera. *Axiom Research Inc.*, 1998-2000.

[47] E.P. Gross. Structure of a Quantized Vortex in Boson Systems. *Nuovo Cimento*, **20**:454, 1961.

[48] E.P. Gross. Hydrodynamics of a Superfluid Condensate. *Jounal of Mathematical Physics*, **4**:195, 1963.

[49] L.P. Pitaevskii. Vortex Lines in an Imperfect Bose Gas. *Sov. Phys. JETP*, **13**:451, 1961.

[50] B. Eiermann, Th. Anker, M. Albiez, M. Taglieber, P. Treutlein, K.-P. Marzlin, and M.K. Oberthaler. Bright Bose-Einstein Gap Solitons of Atoms with Repulsive Interaction. *Physical Review Letters*, **92**:230401, 2004.

[51] T. Tsuzuki. Nonlinear Waves in the Pitaevskii-Gross Equation. *J. Low Temp. Phys.*, **4**:441, 1971.

[52] Th. Busch and J.R. Anglin. Motion of Dark Solitons in Trapped Bose-Einstein Condensates. *Physical Review Letters*, **84**(11):2298, 2000.

[53] Y.S. Kivshar and W. Królikowski. Lagrangian approach for dark solitons. *Opt. Comm.*, **114**:353, 1995.

[54] Th. Busch and J.R. Anglin. Mössbauer effect for dark solitons in Bose-Einstein condensates. *cond-mat/9809408*, 1998.

[55] L. Pitaevskii and S. Stringari. Thermal vs Quantum Decoherence in Double Well Trapped Bose-Einstein Condensates. *Phys. Rev. Letters*, **87**:18, October 2001.

[56] A.S. Sørensen, E. Demler, and M.D. Lukin. Fractional Quantum Hall States of Atoms in Optical Lattices. *Physical Review Letters*, **94**:086803, 2005.

[57] S. Raghavan, A. Smerzi, S. Fantoni, and S.R. Shenoy. Coherent Oscillations Between Two Weakly Coupled Bose-Einstein Condensates: Josephson Effects, π-Oscillations and Macroscopic Self-Trapping. *Physical Review A*, **59**:620–633, 1999.

[58] G. Theocharis, D.J. Frantzeskakis, P.G. Kevrekidis, B.A. Malomed, and Y.S. Kivshar. Ring dark solitons and vortex necklaces in Bose-Einstein condensates. *Physical Review Letters*, **90**:120403, 2003.

Danksagung

Ich möchte mich an dieser Stelle bei allen bedanken, die mich während meines Studiums und meiner Diplomarbeit unterstützt haben:

- Zu allererst möchte ich mich bei meinem Betreuer Prof. Dr. Markus K. Oberthaler für die Aufnahme in seine Arbeitsgruppe bedanken. Seine Begeisterung für die Physik wirkt geradezu ansteckend und sein Bemühen um ein gutes Klima in der Gruppe tragen zu einer angenehmen Arbeitsatmosphäre bei. Danke für das interessante und schöne Jahr!

- Prof. Dr. Christoph Cremer danke ich für die Begutachtung meiner Arbeit.

- Jérôme Estève danke ich für seine ständige Bereitschaft mir bei Problemen helfend unter die Arme zu greifen, besonders wenn es um Matlab-Programme ging. Je vous souhaite, ta femme Bénédicte et toi, les meilleurs vœux pour l'avenir.

- Danke an Rudolf (Rudi) Gati, der immer mit Rat und Tat zur Seite stand und auf alle Fragen geduldig geantwortet hat. Das meiste, was ich über unser Experiment weiß, habe ich von ihm gelernt. Alles Gute für deine Zukunft!

- Andreas Weller und Jens Appmeier danke ich für die angenehme Zeit, die ich mit ihnen im Labor verbringen durfte. Ich wünsche euch weiterhin viel Spaß und gutes Gelingen für die noch anstehende Arbeit.

- Bei Lisa Kierig, Ute Schnorrberger, Karsten Joho und Matthias Weickert, die das Argon- sowie das EIT-Experiment unserer Gruppe betreuen, möchte ich mich ebenfalls für die nette Gruppenatmosphäre bedanken.

- Ich möchte mich auch bei meinem Vorgänger Jonas Fölling bedanken, der dieses Projekt mit auf den Weg gebracht hat. Seine Bereitschaft mir alles zu erklären, was ich zu Beginn wissen musste, hat mir den Einstieg wesentlich erleichtert.

- Während der ersten Hälfte meines Jahres in der Gruppe habe ich mit Börge Hemmerling zusammengearbeitet. Vielen Dank für diese schöne Zeit, sowohl inner- als auch außerhalb des Labors. Ich wünsche dir viel Erfolg für deine Promotion!

- Mein Dank geht auch an die mechanische Werkstatt des Instituts insbesondere an Michael Lutz, der hervorragende Arbeit bei der Fertigung der Objektivfassung geleistet hat.

- Ich möchte mich bei Martina Schürmann und Ruth Barth vom Physikalisch-Chemischen Institut für die unkomplizierte Anfertigung der Rasterelektronenmikroskopaufnahmen, sowie bei Roman Amberger aus der Gruppe von Prof. Cremer für die freundliche Bereitstellung der Mikrometerskala bedanken.
- Den wohl größten Beitrag zum Gelingen meines Studiums und dieser Arbeit haben meine Eltern geleistet, die mich in all meinen Entscheidungen unterstützt haben und mir immer mit Rat zur Seite standen. Vielen Dank!

Erklärung:

Ich versichere, dass ich diese Arbeit selbstständig verfasst und keine anderen als die angegebenen Quellen und Hilfsmittel benutzt habe.

Heidelberg, den _____ _____

Unterschrift